INTERNATIONAL JOURNAL FOR NUMERICAL METHODS IN FLUIDS
Int. J. Numer. Meth. Fluids 2008; **56**:279–303
Published online 30 May 2007 in Wiley InterScience (www.interscience.wiley.com). DOI: 10.1002/fld.1523

Time-linearized time-harmonic 3-D Navier–Stokes shock-capturing schemes

J.-C. Chassaing*,† and G. A. Gerolymos

Institut d'Alembert, Université Pierre-et-Marie-Curie, 75005 Paris, France

SUMMARY

In the present paper, a numerical method for the computation of time-harmonic flows, using the time-linearized compressible Reynolds-averaged Navier–Stokes equations is developed and validated. The method is based on the linearization of the discretized nonlinear equations. The convective fluxes are discretized using an $O(\Delta x_{\mathrm{H}}^3)$ MUSCL scheme with van Leer flux-vector-splitting. Unsteady perturbations of the turbulent stresses are linearized using a frozen-turbulence-Reynolds-number hypothesis, to approximate eddy-viscosity perturbations. The resulting linear system is solved using a pseudo-time-marching implicit ADI-AF (alternating-directions-implicit approximate-factorization) procedure with local pseudo-time-steps, corresponding to a matrix-successive-underrelaxation procedure. The stability issues associated with the pseudo-time-marching solution of the time-linearized Navier–Stokes equations are discussed. Comparison of computations with measurements and with time-nonlinear computations for 3-D shock-wave oscillation in a square duct, for various back-pressure fluctuation frequencies (180, 80, 20 and 10 Hz), assesses the shock-capturing capability of the time-linearized scheme. Copyright © 2007 John Wiley & Sons, Ltd.

Received 8 December 2006; Revised 30 March 2007; Accepted 3 April 2007

KEY WORDS: unsteady flows; time-linearized methods; Navier–Stokes equations; shock-capturing schemes

1. INTRODUCTION

Developments in the prediction of unsteady turbomachinery flows for aeroelastic applications [1] (flutter or forced response), in the last 10 years, have abandoned potential models, and concentrated on 3-D Euler and Navier–Stokes methods [1–16]. Assuming that the vibration amplitudes are small, and that, as a consequence, the unsteady flow can be considered as a small perturbation superimposed on an underlying steady flow, several researchers have contributed to the development of time-linearized time-harmonic methods [17–36] (Table I), which offer substantial gains in

*Correspondence to: J.-C. Chassaing, Institut d'Alembert, Université Pierre-et-Marie-Curie, Case 161, 4 place Jussieu, 75005 Paris, France.
†E-mail: jean-camille.chassaing@upmc.fr

Table I. Review of frequency-domain time-linearized numerical methods based on Euler or Navier–Stokes equations.

Authors	Year	Flow model	Method	Space	Pseudo-time	Turbulence
Ni and Sisto [17]	1976	2-D Euler	LH	MacCormack [37]	Explicit	—
Hall *et al.* [18–21]	1993	3-D Euler	LH	Ni [38]	Ni [38] MLTGRD	—
Lindquist and Giles [22]	1994	1-D Euler	LH	Jameson [39]	RK(4)	—
Ning and He [23]	1998	$2\frac{1}{2}$D Euler	NH	Jameson [39]	RK(4)	—
He *et al.* [24, 30]	1998	2-D NS	NH	Jameson [39]	RK(4)	—
Sreenivas and Witfield [25]	1998	2-D Euler	LH	Roe [40]	LU-SGS [41]	—
Verdon *et al.* [26, 27, 32]	1998	3-D Euler	LH	Roe [40]	LU-SGS [41]	—
Clark and Hall [42, 29]	2000	2-D NS	LH	Ni [38]	IRS + MLTGRD	LSA
Hall *et al.* [33]	2000	2-D Euler	HB	Lax and Wendroff [43]	Explicit	—
Kreiselmaier and Laschka [28]	2000	3-D Euler	LH	Roe [40]	LU-SSOR [44]	—
Chen *et al.* [30]	2001	3-D NS	NH	Jameson [39]	RK(4)	FT
Sbardella and Imregun [31]	2001	3-D NS	LH	UC [31]	Point Jacobi [41]	LSA
Campobasso and Giles [34]	2003	3-D NS	LH	UC [45]	GMRES [41, 46]	LSA
Campobasso and Giles [35]	2004	3-D NS	LH	UC [45]	RPM [47]	LSA
Present	2005	3-D NS	LH	van Leer [48]	ADI-AF [48]	FTS

Notes: NS = Navier–Stokes; LH = linearized-harmonic; NH = nonlinear-harmonic; HB = harmonic-balance; UC = unstructured centered scheme; RK(m) = m-step Runge–Kutta; IRS = implicit residual smoothing; MLTGRD = multigrid acceleration; ADI-AF = alternating-directions-implicit approximately-factored; LU-SSOR = lower–upper symmetric-successive-over-relaxation; LU-SGS = symmetric-Gauss–Seidel; GMRES = gereralized minimal residual [41, 46]; RPM = recursive projection method [47]; LDTS = local-dual-time-stepping; FT = frozen-turbulence; FTS = frozen-turbulence-scale; LSA = linearized version of the Spalart–Allmaras 1-equation model [49].

DOI: 10.1002/fld

computing time, compared to nonlinear methods. This is particularly true for the time-linearized time-harmonic frequency-domain methods, as shown, e.g. by Sreenivas and Witfield [25] whose 2-D time-linearized Euler computations in vibrating cascades were 28 times faster, in the frequency domain, compared to an equivalent time-linearized formulation in the time-domain. The development of accurate shock-capturing schemes combined with the modelling of viscous effects, for the time-linearized equations, is necessary to predict transonic 3-D flows around complex geometries. Additionally, the evaluation of results of time-linearized methods by comparison with results of time-nonlinear methods, and with experimental data, is necessary for assessing the validity and range of applicability of the time-linearized approach.

As early as 1976, Ni and Sisto [17] (Table I) were the first to use the time-linearized Euler equations for the computation of inviscid unsteady flow in flat-plate-cascades at 0-incidence. Hall and Crawley [18] developed a 2-D time-linearized time-harmonic Euler solver based on a nonconservative formulation [50, 51]. In that work [18], transonic flows were addressed by shock-fitting procedures [52, 53], an obvious drawback for the generalization of such methods to 3-D flows over complex geometries. This restriction was removed by Lindquist and Giles [22], who were the first to introduce shock-capturing methods for the time-linearized time-harmonic Euler equations, and to numerically demonstrate that shock-capturing methods predict with acceptable accuracy global aerodynamic effects. These three major contributions [17, 18, 22] stimulated many recent developments on time-linearized time-harmonic methods [19–21, 23–35]. There are two alternatives for the numerical discretization of the time-linearized time-harmonic equations: (1) discretize the nonlinear equations and then linearize the resulting discrete equations, and (2) linearize the equations and then construct a discretization scheme for the linearized flow equations. Hall *et al.* [21] have shown that the two approaches give equivalent results, ensuring the linearized conservation property [21], provided a conservative formulation [50, 51] of the equations is used (this proof was made for the Lax–Wendroff scheme [43]).

Most of these methods [17–35] use a pseudo-time-marching iterative procedure to solve the linearized equations. Nonetheless, a pseudo-time-marching approach, for the linearized equations, may develop numerical instabilities [34, 35, 54], depending on the eigenmodes of the underlying steady flow. Non-pseudo-time-marching approaches are therefore more robust [36, 55].

An original alternative to the time-linearized time-harmonic methods (hereafter LH) was proposed by Ning and He [23, 24] (Table I), where the flow is represented as Fourier-series truncated after the 1-harmonic, so that the time-averaged flow (including the nonlinear effects of the 1-harmonic) is computed simultaneously with the 1-harmonic unsteady perturbation. This time-nonlinear time-harmonic method (hereafter NH) is able to account for nonlinear effects, as do time-marching nonlinear methods, but maintains the computational efficiency of the frequency-domain time-linearized methods. Hall *et al.* [33] maintain higher harmonics in the Fourier-series, using the harmonic balance technique (hereafter HB), which was used to model both nonlinear and linear disturbances in turbomachinery cascades [33]. The resulting coupled partial differential equations for the unknown Fourier-coefficients are solved, in the frequency-domain, using a conventional pseudo-time-marching approach [33].

Following the initial choice of an $O(\Delta x_H^2)$ centred scheme [43] by Lindquist and Giles [22] (who also tested an $O[\Delta x_H]$ van Leer scheme [56] which was obviously too dissipative), many authors [19–21, 23, 24, 29–35] used centred schemes with various artificial dissipation strategies. More recently several authors [25–28, 32, 57–59] developed upwind solvers, based on the linearization of either Roe [40] flux-difference splitting [25–28, 32] or van Leer [56] flux-vector-splitting [57–59], thus avoiding adjustable artificial dissipation coefficients. All of these schemes use the

DOI: 10.1002/fld

MUSCL [60] approach to achieve $O(\Delta x_{\mathrm{H}}^2)$ or $O(\Delta x_{\mathrm{H}}^3)$ accuracy (Δx_{H} is used to denote accuracy in an homogeneous $\Delta x_{\mathrm{H}} = \text{const}$ grid).

For turbulent flows, in a Reynolds-averaged Navier–Stokes (RANS) framework, the linearization of turbulent stresses is an important issue. Several authors [29, 31, 34, 35, 42] solve a linearized form of the 1-equation Spalart–Allmaras [49] ν_{T} model, to estimate the unsteady perturbation of eddy-viscosity. To the authors' knowledge, only Holmes *et al.* [61] have addressed the linearization of a 2-equation $\mathrm{k}-\omega_{\mathrm{T}}$ model [62]. In the present work, we are mainly interested in the numerical scheme, and we have addressed the linearization of turbulent stresses by assuming a Boussinesq hypothesis [63] for the unsteady perturbation of the turbulent stresses, and by neglecting the unsteady perturbations of the turbulence-Reynolds-number (frozen-turbulent-scales approximation, hereafter FTS). Notice that Chen *et al.* [30] have used a frozen eddy-viscosity approximation (hereafter FT) in their calculations of rotor/stator interaction. In a related design-oriented work (Navier–Stokes equations linearized with respect to geometry perturbations), Kim *et al.* [64] have studied the effect of linearizing various 2-equation models (compared to using frozen-turbulence approximations), and have concluded that 'the usual assumption of constant turbulent eddy-viscosity may lead to inaccurate results, particularly in turbulent flows involving strong shocks.' The linearization of the 7-equation Reynolds-stress closure [65] used in the present work for the steady computations [66, 67] is the subject of ongoing research.

The purpose of this work is to develop and evaluate an $O(\Delta x_{\mathrm{H}}^3)$ upwind numerical scheme based on the van Leer flux-splitting formulation, with shock-capturing capability, for the time-linearized time-harmonic 3-D Navier–Stokes equations. The basic strategy is the linearization of schemes used for the time-nonlinear equations, as was done by Lindquist and Giles [22]. Comparison with experiment and time-nonlinear results are presented in the case of a transonic Laval nozzle with a 3-D shock-wave oscillation resulting from a fluctuating back-pressure, for frequencies in the range of [10, 180] Hz.

2. TIME-LINEARIZED NAVIER–STOKES METHODOLOGY

2.1. Nonlinear flow equations and solver

The flow is modelled by the compressible Favre–Reynolds-averaged 3-D Navier–Stokes equations [68], coupled to the six transport equations for the Reynolds-stresses and to the transport equation for the turbulence-kinetic-energy modified-dissipation-rate [68], written symbolically

$$\frac{\partial \underline{w}}{\partial t} + \frac{\partial \underline{F}_\ell}{\partial x_\ell} + \underline{S} \equiv \frac{\partial \underline{w}}{\partial t} + \frac{\partial \underline{F}_x}{\partial x} + \frac{\partial \underline{F}_y}{\partial y} + \frac{\partial \underline{F}_z}{\partial z} + \underline{S} = 0 \tag{1}$$

where

$$\begin{aligned} \underline{w} &= [\underline{w}_{\mathrm{MF}}^{\mathrm{T}}, \underline{w}_{\mathrm{RSM}}^{\mathrm{T}}]^{\mathrm{T}} \\ &= [[\bar{\rho}, \bar{\rho}\tilde{u}, \bar{\rho}\tilde{v}, \bar{\rho}\tilde{w}, \bar{\rho}\check{h}_t - \bar{p}], [\bar{\rho}\widetilde{u''u''}, \bar{\rho}\widetilde{u''v''}, \bar{\rho}\widetilde{v''v''}, \bar{\rho}\widetilde{v''w''}, \bar{\rho}\widetilde{w''w''}, \bar{\rho}\widetilde{w''u''}, \bar{\rho}\varepsilon^*]]^{\mathrm{T}} \in \mathbb{R}^{12} \end{aligned} \tag{2}$$

is the vector of unknowns, $\underline{w}_{\mathrm{MF}} \in \mathbb{R}^5$ is the vector of mean-flow-variables, $\underline{w}_{\mathrm{RSM}} \in \mathbb{R}^7$ is the vector of turbulence-variables (Reynolds-stresses and dissipation-rate), $\underline{F}_\ell \in \mathbb{R}^{12}$ ($\underline{F}_x$, $\underline{F}_y$, $\underline{F}_z$) are the combined convective ($\underline{F}_\ell^{\mathrm{C}}$) and diffusive (viscous; $\underline{F}_\ell^{\mathrm{V}}$) fluxes ($\underline{F}_\ell = \underline{F}_\ell^{\mathrm{C}} + \underline{F}_\ell^{\mathrm{V}}$), $\underline{S} \in \mathbb{R}^{12}$ are

DOI: 10.1002/fld

the source-terms, t is the time, x_ℓ (x, y, z) are the Cartesian space coordinates, u_ℓ (u, v, w) are the velocity components, ρ is the density, p is the pressure, $\breve{h}_t = \tilde{h} + \frac{1}{2}\tilde{u}_i\tilde{u}_i$ is the total enthalpy of the mean-flow, h is the specific enthalpy, and ε^* is the modified [69] dissipation-rate ($\varepsilon^* = \varepsilon - 2\breve{\nu}[\mathrm{grad}(\sqrt{\mathrm{k}})]^2$), ε is the dissipation-rate, $\mathrm{k} = \frac{1}{2}\widetilde{u_i''u_i''}$ is the turbulence-kinetic-energy, and ν is the kinematic viscosity. The symbol $(\tilde{\cdot})$ indicates Favre-averaging, $(\bar{\cdot})$ nonweighted-averaging, $(\cdot'')$ Favre-fluctuations, and $(\cdot')$ nonweighted-fluctuations. The symbol $(\breve{\cdot})$ is used to denote a function of average quantities which is neither a Favre-average nor a nonweighted average. The exact expressions of the fluxes $\underline{F}_\ell$ and of the source-terms $\underline{S}$ depend on the particular model used, and are given in the corresponding references [65, 66, 68, 70]. Notice that all of the source-terms for the mean-flow-equations are 0, except for the mean-flow-energy equation, for which the source-term $-S_{\breve{h}_t}$ is the sum of turbulence-related quantities [68, 70] which appear in the turbulence-kinetic-energy equation ($-S_{\breve{h}_t}$ is generally small even for supersonic [$M<5$] wall-bounded flows).

These equations are solved using an $O(\Delta x_{\mathrm{H}}^3)$ upwind-biased scheme (with van Leer [56] flux-vector-splitting and the Anderson *et al.* [48] implementation of the van Albada [71] limiter), with implicit $O(\Delta t)$ LDTS (local-dual-time-stepping) subiterations [66], augmented with mean-flow-multigrid acceleration [67]. For unsteady flows, an $O(\Delta t^2)$ implicit DTS (dual-time-stepping) methodology is used, with subiterations, whose number is determined dynamically, based on an increment-convergence-tolerance criterion [72].

2.2. Basic linearization strategy

The time-linearized time-harmonic equations are obtained by considering small unsteady time-harmonic perturbations ${}^1\underline{w}(x, y, z, t)$ of the conservative variables $\underline{w}$, around an underlying steady flow ${}^0\underline{w}(x, y, z)$:

$$\underline{w}(x, y, z, t) = {}^0\underline{w}(x, y, z) + {}^1\underline{w}(x, y, z, t) = {}^0\underline{w}(x, y, z) + \Re[{}^1\underline{\hat{w}}(x, y, z)\, \mathrm{e}^{\mathrm{i}2\pi f t}] \tag{3}$$

where ${}^1\underline{\hat{w}}(x, y, z) \in \mathbb{C}^{12}$ are the harmonics of the conservative variables and f is the frequency. Any quantity $Q = Q(\underline{w}, \mathrm{grad}\,\underline{w})$, appearing in the nonlinear differential or discretized equations, is linearized as

$$\begin{aligned} {}^1\hat{Q}({}^0\underline{\hat{w}}, \mathrm{grad}\,{}^0\underline{w}; {}^1\underline{\hat{w}}, \mathrm{grad}\,{}^1\underline{\hat{w}}) \\ = \left[\frac{\partial Q}{\partial \underline{w}}({}^0\underline{w}, \mathrm{grad}\,{}^0\underline{w})\right] {}^1\underline{\hat{w}} + \left[\frac{\partial Q}{\partial\, \mathrm{grad}\,\underline{w}}({}^0\underline{w}, \mathrm{grad}\,{}^0\underline{w})\right] \mathrm{grad}\,{}^1\underline{\hat{w}} \end{aligned} \tag{4}$$

2.3. Finite-volume discretization

The numerical scheme for the time-linearized equations is obtained directly by linearization of the corresponding scheme for the time-nonlinear equations (Equation (1)) [21, 22, 28]. The nonlinear scheme used in the present work, is a finite-volume MUSCL [60] scheme, with van Leer flux-vector-splitting [56] and the Anderson *et al.* [48] implementation of the van Albada [71] limiter, which is described in detail in Chassaing *et al.* [66]. Assuming that the equations are discretized on a time-independent structured grid, and noting (ξ, η, ζ) the grid-directions (i, j, k), $({}^\xi\mathscr{S}_{i\pm1/2,j,k}, {}^\eta\mathscr{S}_{i,j\pm1/2,k}, {}^\zeta\mathscr{S}_{i,j,k\pm1/2})$ the cell-face areas of the staggered-grid-cell around the point (i, j, k), and $([{}^\xi n_x, {}^\xi n_y, {}^\xi n_z]^{\mathrm{T}}_{i\pm1/2,j,k}, [{}^\eta n_x, {}^\eta n_y, {}^\eta n_z]^{\mathrm{T}}_{i,j\pm1/2,k}, [{}^\zeta n_x, {}^\zeta n_y, {}^\zeta n_z]^{\mathrm{T}}_{i,j,k\pm1/2})$

DOI: 10.1002/fld

the corresponding unit-normals (positive in the positive grid direction), the discrete scheme for the time-linearized time-harmonic equations, obtained by linearization of the corresponding nonlinear discrete scheme (Equation (6) of Chassaing *et al.* [66]), reads

$$\mathrm{i}2\pi f\,{}^1\underline{\hat{w}}_{\mathrm{MF}_{i,j,k}} + \frac{1}{\mathscr{V}_{i,j,k}}\begin{bmatrix} +{}^{\xi}\mathscr{S}_{i+1/2,j,k}\,{}^{\xi}[{}^1\underline{\hat{F}}^{\mathrm{N}}_{\mathrm{MF}}]_{i+1/2,j,k} - {}^{\xi}\mathscr{S}_{i-1/2,j,k}\,{}^{\xi}[{}^1\underline{\hat{F}}^{\mathrm{N}}_{\mathrm{MF}}]_{i-1/2,j,k} \\ +{}^{\eta}\mathscr{S}_{i,j+1/2,k}\,{}^{\eta}[{}^1\underline{\hat{F}}^{\mathrm{N}}_{\mathrm{MF}}]_{i,j+1/2,k} - {}^{\eta}\mathscr{S}_{i,j-1/2,k}\,{}^{\eta}[{}^1\underline{\hat{F}}^{\mathrm{N}}_{\mathrm{MF}}]_{i,j-1/2,k} \\ +{}^{\zeta}\mathscr{S}_{i,j,k+1/2}\,{}^{\zeta}[{}^1\underline{\hat{F}}^{\mathrm{N}}_{\mathrm{MF}}]_{i,j,k+1/2} - {}^{\zeta}\mathscr{S}_{i,j,k-1/2}\,{}^{\zeta}[{}^1\underline{\hat{F}}^{\mathrm{N}}_{\mathrm{MF}}]_{i,j,k-1/2} \end{bmatrix}$$

$$+[{}^1\underline{\hat{S}}_{\mathrm{MF}}]_{i,j,k} \equiv \mathrm{i}2\pi f\,{}^1\underline{\hat{w}}_{\mathrm{MF}_{i,j,k}} + {}^1\underline{\hat{\mathscr{L}}}_{\mathrm{MF}_{i,j,k}} \cong 0 \tag{5}$$

where $\mathscr{V}_{i,j,k}$ is the control-volume. The perturbation of numerical flux ${}^1\underline{\hat{F}}^{\mathrm{N}}_{\mathrm{MF}}$ is given by

$${}^{\xi}[{}^1\underline{\hat{F}}^{\mathrm{N}}_{\mathrm{MF}}]_{i\pm1/2,j,k} = \left[{}^{\xi}\left({}^1\underline{\hat{F}}^{\mathrm{CN}}_{\mathrm{MF}}\right) + {}^1\underline{\hat{F}}^{\mathrm{VN}}_{\mathrm{MF}_\ell}\,{}^{\xi}n_\ell\right]_{i\pm1/2,j,k} \tag{6}$$

where $\underline{F}^{\mathrm{CN}}_{\mathrm{MF}}$ is the convective numerical flux [66], and $\underline{F}^{\mathrm{CV}}_{\mathrm{MF}}$ is the viscous numerical flux [66].

2.4. Linearization and approximation of the viscous fluxes and of the source-term

The numerical viscous fluxes at the staggered-grid cell-faces are given by

$$[{}^1\underline{\hat{F}}^{\mathrm{VN}}_{\mathrm{MF}_\ell}]_{i\pm1/2,j,k} = \tfrac{1}{2}([{}^1\underline{\hat{F}}^{\mathrm{V}}_{\mathrm{MF}_\ell}]_{i,j,k} + [{}^1\underline{\hat{F}}^{\mathrm{V}}_{\mathrm{MF}_\ell}]_{i\pm1,j,k}) \tag{7}$$

resulting in a centred $O(\Delta x_{\mathrm{H}}^2)$ scheme for the viscous terms (the derivatives involved in the evaluation of $[{}^1\underline{\hat{F}}^{\mathrm{V}}_{\mathrm{MF}_\ell}]_{i,j,k}$ are computed using an $O(\Delta x_{\mathrm{H}}^2)$ scheme [73]). To uncouple the time-linearized time-harmonic mean-flow equations (Equation (5)) from the equations for the unsteady perturbations of the Reynolds-stresses (and thus reduce the number of equations from 12 to only 5), the unsteady perturbations of the Reynolds-stresses and of the turbulent-heat-flux must be modelled using only steady quantities and mean-flow-perturbations. Details on the approximations used for the viscous terms, and on the frozen-turbulence-scales assumption used to evaluate the perturbations of the Reynolds-stresses and of the turbulent-heat-fluxes are given in Appendix A:

$$[{}^1\underline{\hat{F}}^{\mathrm{V}}_{\mathrm{MF}_\ell}] \cong [{}^1\underline{\hat{F}}^{\mathrm{V}}_{\mathrm{MF}_\ell}]({}^0\underline{\hat{w}}, \mathrm{grad}\,{}^0\underline{w}; {}^1\underline{\hat{w}}_{\mathrm{MF}}, \mathrm{grad}\,{}^1\underline{\hat{w}}_{\mathrm{MF}}) \quad [{}^1\underline{\hat{S}}_{\mathrm{MF}}] \cong 0 \tag{8}$$

where ${}^1\underline{\hat{F}}^{\mathrm{V}}_{\mathrm{MF}_\ell}$ is given in Appendix A.

2.5. Linearization of the convective fluxes

The unsteady perturbations of the convective numerical fluxes (Equations (5) and (6)), on a time-independent grid, can be written as

$${}^1\underline{\hat{F}}^{\mathrm{CN}}_{\mathrm{MF}}({}^0\underline{w}^{\pm}_{\mathrm{MF}}, {}^1\underline{\hat{w}}^{\pm}_{\mathrm{MF}}; n_x, n_y, n_z) = \left[\frac{\partial \underline{F}^{+}_{\mathrm{MF}}}{\partial \underline{w}^{-}_{\mathrm{MF}}}({}^0\underline{w}^{-}_{\mathrm{MF}}; n_x, n_y, n_z)\right] {}^1\underline{\hat{w}}^{-}_{\mathrm{MF}}$$

$$+ \left[\frac{\partial \underline{F}^{-}_{\mathrm{MF}}}{\partial \underline{w}^{+}_{\mathrm{MF}}}({}^0\underline{w}^{+}_{\mathrm{MF}}; n_x, n_y, n_z)\right] {}^1\underline{\hat{w}}^{+}_{\mathrm{MF}} \tag{9}$$

DOI: 10.1002/fld

where $\underline{w}_{\mathrm{MF}}^{\mathrm{L}} \equiv \underline{w}_{\mathrm{MF}}^{-}$ and $\underline{w}_{\mathrm{MF}}^{\mathrm{R}} \equiv \underline{w}_{\mathrm{MF}}^{+}$ are the MUSCL-reconstructed conservative-variables at the interface [60], $\underline{F}_{\mathrm{MF}}^{\pm}$ are the van Leer split-fluxes [48, 56, 66], and the corresponding flux Jacobians $\partial \underline{F}_{\mathrm{MF}}^{\pm}/\partial \underline{w}_{\mathrm{MF}}^{\mp}$ are computed by straightforward differentiation (the exact expressions can be found, e.g. in Vallet [74]). Notice, however, that the expression of the van Leer fluxes (Equations (7)–(9) in Chassaing *et al.* [66]) depends on the normal-to-the-cell-interface Mach-number $M_n^{\pm} = u_i^{\pm} n_i (a^{\pm})^{-1}$, computed with the appropriate MUSCL variables (different expressions depending on whether $(\pm M_n^{\pm} < -1,\ |\pm M_n^{\pm}| < 1,\ \pm M_n^{\pm} > +1)$. This dependence on $M_n^{\pm}$ is not differentiated when computing the flux-Jacobians $\partial \underline{F}_{\mathrm{MF}}^{\pm}/\partial \underline{w}_{\mathrm{MF}}^{\mp}$ (Equation (9)).

The MUSCL-variables, for the time-nonlinear $O(\Delta x_{\mathrm{H}}^3)$ scheme used in the present work, are obtained by the MUSCL interpolation function [66]:

$$\hat{\underline{w}}_{\mathrm{MF}}^{\pm} = \underline{\mathrm{w}}_{\mathrm{MF}}^{\pm}([\underline{w}_{\mathrm{MF}}]_{-1}, [\underline{w}_{\mathrm{MF}}]_0, [\underline{w}_{\mathrm{MF}}]_{+1}; \underline{s}_{\mathrm{MF}}) \tag{10}$$

where the indices $-1, 0$, and $+1$ denote the points in the stencil and $\underline{s}_{\mathrm{MF}} \in \mathbb{R}^5$ is the slope-limiter [56] computed on the same stencil. When computing the unsteady perturbations of the MUSCL variables, the limiters are not differentiated, a practice also followed by other authors [28, 57]. The corresponding MUSCL variables for the Fourier coefficients of the perturbations of the variables are given by

$${}^1\hat{\underline{w}}_{\mathrm{MF}}^{\pm} = \underline{\mathrm{w}}_{\mathrm{MF}}^{\pm}([{}^1\hat{\underline{w}}_{\mathrm{MF}}]_{-1}, [{}^1\hat{\underline{w}}_{\mathrm{MF}}]_0, [{}^1\hat{\underline{w}}_{\mathrm{MF}}]_{+1}; {}^0\underline{s}_{\mathrm{MF}}) \tag{11}$$

where ${}^0\underline{s}_{\mathrm{MF}}$ is computed on the same stencil, but using the steady flow variables ${}^0\underline{w}$. In the present work the Anderson *et al.* [48] implementation of the van Albada *et al.* [71] limiter is used (cf. Appendix B).

This approach of using the underlying steady-flow to compute the limiters for the MUSCL reconstruction works quite well, and has been used by many authors [25–28, 32, 57–59]. Nonetheless, it results in a reconstruction which is linear in ${}^1\hat{\underline{w}}_{\mathrm{MF}}$ (Equation (11)). As discussed by van Leer [75], by virtue of the famous Godunov theorem, a linear MUSCL discretization scheme of $O(\Delta x^r)$ with $r > 1$ is not monotonicity preserving. The alternative approach of constructing limiters based on ${}^1\hat{\underline{w}}_{\mathrm{MF}}$ only (so as to construct a nonlinear MUSCL reconstruction) was also tested, and gave results very similar with the previous approach.

2.6. Linear system solution

Assembling the time-linearized equations (Equations (5)–(11)) results in the linear system

$$\mathrm{i}2\pi f\, {}^1\hat{\mathfrak{w}}_{\mathrm{MF}} + {}^1\hat{\mathfrak{L}}_{\mathrm{MF}}({}^0\mathfrak{w}, {}^1\hat{\mathfrak{w}}_{\mathrm{MF}}) \equiv \mathrm{i}2\pi f\, {}^1\hat{\mathfrak{w}}_{\mathrm{MF}} + \mathbf{A}_{\mathrm{MF}}({}^0\mathfrak{w})\, {}^1\hat{\mathfrak{w}}_{\mathrm{MF}} = 0 \tag{12}$$

where ${}^0\mathfrak{w} = [{}^0\underline{w}_{1,1,1}, {}^0\underline{w}_{1,1,2}, \ldots, {}^0\underline{w}_{N_i,N_j,N_k}]^{\mathrm{T}} \in \mathbb{R}^{12\times N_i\times N_j\times N_k}$ is the global vector of the unperturbed conservative variables, ${}^1\hat{\mathfrak{w}}_{\mathrm{MF}} = [{}^1\hat{\underline{w}}_{\mathrm{MF}_{1,1,1}}, {}^1\hat{\underline{w}}_{\mathrm{MF}_{1,1,2}}, \ldots, {}^1\hat{\underline{w}}_{\mathrm{MF}_{N_i,N_j,N_k}}]^{\mathrm{T}} \in \mathbb{C}^{5\times N_i\times N_j\times N_k}$ is the global vector of unknowns and ${}^1\hat{\mathfrak{L}}_{\mathrm{MF}} = [{}^1\hat{\mathscr{L}}_{\mathrm{MF}_{1,1,1}}, {}^1\hat{\mathscr{L}}_{\mathrm{MF}_{1,1,2}}, \ldots, {}^1\hat{\mathscr{L}}_{\mathrm{MF}_{Ni,Nj,Nk}}]^{\mathrm{T}} \in \mathbb{C}^{5\times N_i\times N_j\times N_k}$ is the global linear space-operator (Equation (5)), and $\mathbf{A}_{\mathrm{MF}}({}^0\mathfrak{w}) \in \mathbb{R}^{(5\times N_i\times N_j\times N_k)\times(5\times N_i\times N_j\times N_k)}$ is the matrix associated with ${}^1\hat{\mathfrak{L}}_{\mathrm{MF}}$ (${}^1\hat{\mathfrak{L}}_{\mathrm{MF}} \equiv \mathbf{A}_{\mathrm{MF}}\, {}^1\hat{\mathfrak{w}}_{\mathrm{MF}}$). As originally suggested by Ni and Sisto [17], the time-linearized time-harmonic equations (Equation (12)) are marched in a pseudo-time t^* until

DOI: 10.1002/fld

convergence of the unknowns ${}^1\hat{\mathfrak{w}}_{\mathrm{MF}}$:

$$\frac{\mathrm{d}^1\hat{\mathfrak{w}}_{\mathrm{MF}}}{\mathrm{d}t^*} + \mathrm{i}2\pi f\,{}^1\hat{\mathfrak{w}}_{\mathrm{MF}} + \mathbf{A}_{\mathrm{MF}}({}^0\mathfrak{w})\,{}^1\hat{\mathfrak{w}}_{\mathrm{MF}} = 0 \tag{13}$$

Using an $O(\Delta t^*)$ backward-Euler [76] scheme for the pseudo-time integration yields, at iteration n, the following implicit formulation:

$$\{\mathbf{I} + \Delta\mathbf{t}^*\ [\mathrm{i}2\pi f\mathbf{I} + \mathbf{A}^{\mathrm{J}}_{\mathrm{MF}}({}^0\mathfrak{w})]\}^{(n)}[\Delta\,{}^1\hat{\mathfrak{w}}_{\mathrm{MF}}] \cong -\Delta\mathbf{t}^*\ [\mathrm{i}2\pi f\mathbf{I} + \mathbf{A}_{\mathrm{MF}}({}^0\mathfrak{w})]^{(n)}[{}^1\hat{\mathfrak{w}}_{\mathrm{MF}}] \tag{14}$$

where ${}^{(n)}[{}^1\hat{\mathfrak{w}}_{\mathrm{MF}}]$ denotes the global vector of unknowns at iteration n, ${}^{(n)}[\Delta\,{}^1\hat{\mathfrak{w}}_{\mathrm{MF}}] = {}^{(n+1)}[{}^1\hat{\mathfrak{w}}_{\mathrm{MF}}] - {}^{(n)}[{}^1\hat{\mathfrak{w}}_{\mathrm{MF}}]$ is the increment between iterations n and $n+1$, $\mathbf{I} \in \mathbb{R}^{(5\times Ni\times Nj\times Nk)\times(5\times Ni\times Nj\times Nk)}$ is the identity matrix, $\Delta\mathbf{t}^* = \mathrm{diag}[(\Delta t^*_{1,1,1})\underline{\underline{I}}_5, (\Delta t^*_{1,1,2})\underline{\underline{I}}_5, \ldots, (\Delta t^*_{N_i,N_j,N_k})\underline{\underline{I}}_5]$ is the diagonal matrix associated with the local pseudo-time-steps $\Delta t^*_{i,j,k}$, $\underline{\underline{I}}_5$ is the 5×5 identity matrix, and the matrix $\mathbf{A}^{\mathrm{J}}_{\mathrm{MF}}$ is an appropriate approximation of the matrix $\mathbf{A}_{\mathrm{MF}}$ chosen to reduce computational time. Note that defining $\Delta t^{**}_{i,j,k} = \Delta t^*_{i,j,k}/(1 + \mathrm{i}2\pi f\Delta t^*_{i,j,k})$ $(\Delta t^{**}_{i,j,k} \in \mathbb{C})$, with associated diagonal matrix $\Delta\mathbf{t}^{**}$, Equation (14) can be simplified as

$$\{\mathbf{I} + \Delta\mathbf{t}^{**}\ \mathbf{A}^{\mathrm{J}}_{\mathrm{MF}}({}^0\mathfrak{w})\}^{(n)}[\Delta\,{}^1\hat{\mathfrak{w}}_{\mathrm{MF}}] \cong -\Delta\mathbf{t}^{**}\ [\mathrm{i}2\pi f\mathbf{I} + \mathbf{A}_{\mathrm{MF}}({}^0\mathfrak{w})]^{(n)}[{}^1\hat{\mathfrak{w}}_{\mathrm{MF}}] \tag{15}$$

Following work on the solution of the nonlinear Navier–Stokes equations [67, 66], the iteration matrix $\mathbf{A}^{\mathrm{J}}_{\mathrm{MF}}$ used in the present work is obtained as the Jacobian of an approximate space operator ${}^1\hat{\mathfrak{L}}^{\mathrm{J}}_{\mathrm{MF}}$, which uses $O(\Delta x_{\mathrm{H}})$ discretization for the convective fluxes and an *ad hoc* spectral radius approximation for the viscous terms [66, 67, 74]. The resulting matrix $(\mathbf{I} + \Delta\mathbf{t}^{**}\ \partial\,{}^1\hat{\mathfrak{L}}^{\mathrm{J}}_{\mathrm{MF}}/\partial\,{}^1\hat{\mathfrak{w}}_{\mathrm{MF}})$ is further approximately factored [48, 77] $(\mathbf{I} + \Delta\mathbf{t}^{**}\mathbf{A}^{\mathrm{J}}_{\mathrm{MF}}) \cong (\mathbf{I} + \Delta\mathbf{t}^{**\xi}\mathbf{A}^{\mathrm{J}}_{\mathrm{MF}})(\mathbf{I} + \Delta\mathbf{t}^{**\eta}\mathbf{A}^{\mathrm{J}}_{\mathrm{MF}})(\mathbf{I} + \Delta\mathbf{t}^{**\zeta}\mathbf{A}^{\mathrm{J}}_{\mathrm{MF}})$ to obtain an alternating directions implicit (ADI) solution [48, 77, 78] of the linear system (Equation (15))

$$\begin{aligned}
(\mathbf{I} + \Delta\mathbf{t}^{**\xi}\mathbf{A}^{\mathrm{J}}_{\mathrm{MF}})^{(n,\xi)}[\Delta^1\hat{\mathfrak{w}}_{\mathrm{MF}}] &= -\Delta\mathbf{t}^{**}[\mathrm{i}2\pi f\mathbf{I} + \mathbf{A}_{\mathrm{MF}}({}^0\mathfrak{w})]^{(n)}[{}^1\hat{\mathfrak{w}}_{\mathrm{MF}}]\\
(\mathbf{I} + \Delta\mathbf{t}^{**\eta}\mathbf{A}^{\mathrm{J}}_{\mathrm{MF}})^{(n,\eta)}[\Delta\,{}^1\hat{\mathfrak{w}}_{\mathrm{MF}}] &= {}^{(n,\xi)}[\Delta\,{}^1\hat{\mathfrak{w}}_{\mathrm{MF}}]\\
(\mathbf{I} + \Delta\mathbf{t}^{**\zeta}\mathbf{A}^{\mathrm{J}}_{\mathrm{MF}})^{(n,\zeta)}[\Delta\,{}^1\hat{\mathfrak{w}}_{\mathrm{MF}}] &= {}^{(n,\eta)}[\Delta\,{}^1\hat{\mathfrak{w}}_{\mathrm{MF}}]\\
{}^{(n)}[\Delta\,{}^1\hat{\mathfrak{w}}_{\mathrm{MF}}] &= {}^{(n,\zeta)}[\Delta\,{}^1\hat{\mathfrak{w}}_{\mathrm{MF}}]\\
{}^{(n+1)}[{}^1\hat{\mathfrak{w}}_{\mathrm{MF}}] &= \mathbf{B}\{{}^{(n)}[{}^1\hat{\mathfrak{w}}_{\mathrm{MF}}] + {}^{(n)}[\Delta\,{}^1\hat{\mathfrak{w}}_{\mathrm{MF}}]\}
\end{aligned} \tag{16}$$

where the operator $\mathbf{B}$ corresponds to the explicit application of boundary-conditions (cf. Appendix C). The real matrices ${}^{\xi}\mathbf{A}^{\mathrm{J}}_{\mathrm{MF}}$, ${}^{\eta}\mathbf{A}^{\mathrm{J}}_{\mathrm{MF}}$, and ${}^{\zeta}\mathbf{A}^{\mathrm{J}}_{\mathrm{MF}}$, are given in Vallet [74]. They include the implicit application of boundary-conditions following the method of Chakravarthy [74, 79]. The three successive spacewise linear systems are solved using banded-LU factorization [80] (with appropriate rearrangement of the storage order of the matrices and increment vectors [48, 78]) with corresponding bandwidth of $(1 + 2\times 9)$. The local pseudo-time-steps $\Delta t^*_{i,j,k}$ are computed using the same formula as for nonlinear computations (cf. Equation (28) in Chassaing *et al.* [66]; in the present computations CFL = VNN = 20 was used).

DOI: 10.1002/fld

Although the matrices ${}^{\xi}\mathbf{A}^{\mathrm{J}}_{\mathrm{MF}}$, ${}^{\eta}\mathbf{A}^{\mathrm{J}}_{\mathrm{MF}}$, and ${}^{\zeta}\mathbf{A}^{\mathrm{J}}_{\mathrm{MF}}$, are real, $\Delta t^{**}\in\mathbb{C}$, so that the LU-factorization [80] is concerned with a complex matrix (more real operations than for a real matrix of the same size). In many applications, such as those considered in the present paper, the following condition holds:

$$|i\omega\Delta t^{*}| \ll 1 \quad \Rightarrow \quad \Delta t^{**} \cong \Delta t^{*} \in \mathbb{R} \tag{17}$$

In these cases, $\Delta t^{**} \in \mathbb{C}$ is replaced by $\Delta t^{*} \in \mathbb{R}$ in Equations (15) and (16), so that the LU-factorization [80] is performed for real matrices, and only the back-substitution [80] involves complex numbers, resulting in an important speed-up (back-substitution is quite inexpensive compared to the LU-factorization [80]).

In the present numerical implementation, the time-linearized space-operator ${}^{1}\hat{\mathfrak{L}}_{\mathrm{MF}}({}^{0}\mathfrak{w}, {}^{1}\hat{\mathfrak{w}}_{\mathrm{MF}})$ and the Jacobian matrices ${}^{\xi}\mathbf{A}$, ${}^{\eta}\mathbf{A}$, ${}^{\zeta}\mathbf{A}$, are evaluated at each iteration (in the same way as for nonlinear methods). An alternative to this, which was initially tested, is to compute and store in computer memory the coefficients of the matrix $\mathbf{A}_{\mathrm{MF}}$, and then use them to compute ${}^{1}\hat{\mathfrak{L}}_{\mathrm{MF}} \equiv \mathbf{A}_{\mathrm{MF}}{}^{1}\hat{\mathfrak{w}}_{\mathrm{MF}}$. Although this procedure reduces computing time by 15%, it requires an order-of-magnitude larger computer memory [59], which becomes prohibitively large for realistic 3-D applications (typically, for a 10^6 points grid, 10 Gb of memory are required for the non-zero coefficients of $\mathbf{A}_{\mathrm{MF}}$), and was therefore not retained.

3. TRANSONIC NOZZLE WITH FLUCTUATING BACK-PRESSURE

3.1. Configuration studied

The time-linearized time-harmonic method is evaluated through comparison with measurements [81, 82] and with previous time-nonlinear computations [72, 83] in a 3-D nozzle experimentally and computationally investigated by Ott *et al.* [82] (Figure 1). The facility, with a width of 40 mm, was equipped with nozzle liners giving a converging-diverging section. The unsteady flow is created by the rotation of a cylindrical rod of elliptical cross-section (situated 480 mm downstream of the throat), which induces the oscillation of the shock-wave in the divergent section of the nozzle. The fluctuating back-pressure frequencies can be varied between 0 and 180 Hz. Unsteady pressures were measured by unsteady pressure transducers located on the side-wall, at its intersection with the y-symmetry plane of the nozzle, and placed 5 mm apart, in the shock wave neighbourhood. Experimental conditions are [81–83]

$$\begin{aligned} &p_{t_i} = 168\,600\,\mathrm{Pa}, \quad T_{t_i} = 323\,\mathrm{K}, \quad \delta_{y_i} = 0.5\,\mathrm{mm}, \quad \delta_{z_i} = 5\,\mathrm{mm} \\ &T_{u_i} = 1.6\%, \quad \ell_{T_i} = 0.3\,\mathrm{mm}, \quad {}^{0}\breve{M}_{\mathrm{SW}} \cong 1.2 \end{aligned} \tag{18}$$

where δ_{y_i} is the boundary-layer thickness at inflow on the nozzle-liners, δ_{z_i} the boundary-layer thickness at inflow on the sidewall, p_{t_i} the inflow-total-pressure outside the boundary-layers, T_{t_i} the inflow-total-temperature outside the boundary-layers, T_{u_i} the turbulence-intensity at inflow, ℓ_{T_i} the turbulence-length-scale at inflow, and ${}^{0}\breve{M}_{\mathrm{SW}}$ is the shock-wave Mach-number of the underlying steady-flow.

For this configuration, the shock-wave position and the post-shock pressure-recovery cannot be predicted by 2-D computations [82–84]. Indeed, because of the relatively small width of the nozzle and the rather thick sidewall boundary-layers, only 3-D viscous computations can correctly predict this flow, where the shock-wave position is dominated by the corner-flow/shock-wave

DOI: 10.1002/fld

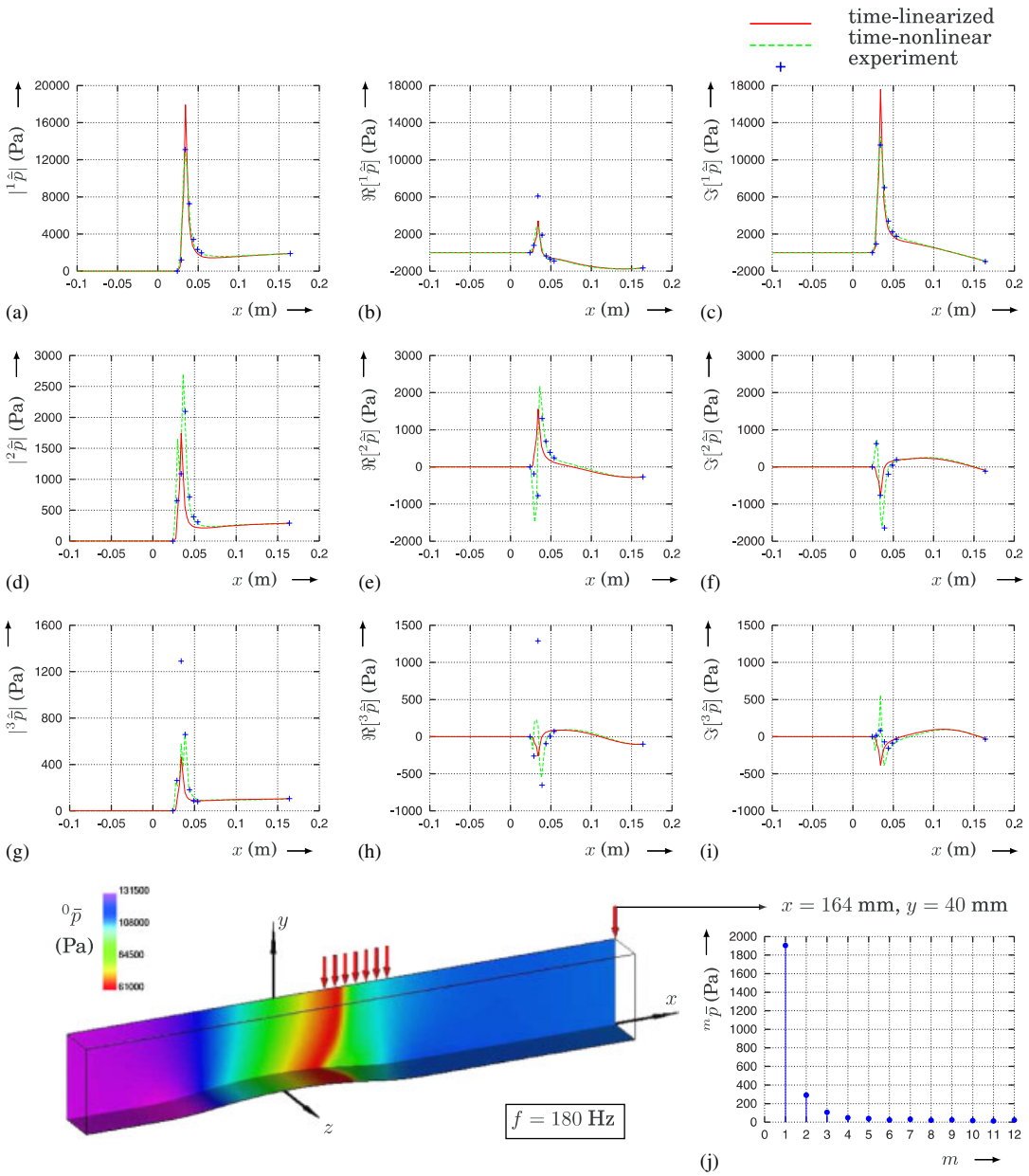

Figure 1. Steady RSM–RANS computation [66] wall-pressure-levels, harmonics of measured outflow-pressure-signal (j), and comparison of time-linearized time-harmonic computations for $f = 180\,\mathrm{Hz}$ (x-wise distributions of amplitude, real, and imaginary part of ${}^1\hat{\bar{p}}$, ${}^2\hat{\bar{p}}$, and ${}^3\hat{\bar{p}}$) with measurements [81, 82] (pressure-probes indicated by the solid red arrows) and with time-nonlinear RSM–RANS computations [72] for the Ott *et al.* [82] nozzle (grid_A [72]).

DOI: 10.1002/fld

Table II. Back-pressure harmonics for different frequencies.

Frequency (Hz)	$\lvert^1\hat{p}_o\rvert$ (Pa)	$\angle^1\hat{p}_o$	$\lvert^2\hat{p}_o\rvert$ (Pa)	$\angle^2\hat{p}_o$	$\lvert^3\hat{p}_o\rvert$ (Pa)	$\angle^3\hat{p}_o$
180	1903.201	−60.86°	292.55	46.30°	107.880	39.25°
80	2346.173	−130.19°	274.69	70.73°	89.470	55.99°
20	2710.683	−18.08°	207.16	−30.22°	72.022	2.86°
10	2710.683	−18.08°	207.16	−30.22°	72.022	2.86°

interaction [83]. Previous RANS time-nonlinear computations [72, 83], using both 2-equation [83] and RSM [72] turbulence closures, are in quite satisfactory agreement with measurements. The computational grids used ($121 \times 57 \times 49$ grid_A, $201 \times 57 \times 49$ grid_B, and $201 \times 111 \times 91$ grid_C) are the same as those used in previous time-nonlinear computations [72, 83], (they are described in detail in Table III in Chassaing *et al.* [72]). For all of these grids, the nondimensional distance of the first grid-point away from the wall is $\Delta y_w^+ \cong \Delta z_w^+ \cong 0.5$.

3.2. Computational procedure

The time-linearized time-harmonic computations were run with an underlying steady-flow computed by a steady RSM–RANS solver [66] using the WNF–LSS RSM [65]. The boundary conditions were described previously (Equations (18), Appendix C).

At the outflow-boundary location ($x = x_o = 164$ mm), the pressure-signal was measured in the experiment. It can be Fourier-series expanded

$$\bar{p}(t, x_o, y, z) = p_o(t) = {}^0p_o + \sum_{m=1}^{12} [\lvert^m\hat{p}_o\rvert \cos(2\pi m f t + {}^m\varphi_o)] \quad \forall y, z \tag{19}$$

where ${}^0p_o$, is the time-mean outflow pressure, $\lvert^m\hat{p}_o\rvert$ and ${}^m\varphi_o$ the amplitudes and phase-angles of the Fourier-coefficients, and m the harmonic number (12 harmonics were considered [84]). Processing the experimental signals for $f = 20, 80, 180$ Hz indicates [84] that the first three harmonics ($m = 1, 2, 3$) are sufficient to describe the back-pressure variation (Table II).

Contrary to the time-nonlinear computations [72, 83], where the instantaneous pressure signal (Equation (19)) is imposed at the outflow boundary, time-harmonic time-linearized computations can only be run for a single frequency (yielding information only on the 1-harmonic corresponding to this frequency). Neglecting the nonlinear interactions between harmonics, the time-linearized computational procedure consists of running three separate computations, one for each of the first three harmonics (Equation (19)):

$$\begin{aligned}
\underline{w}_{(1)}(x, y, z, t) &= {}^0\underline{w}(x, y, z) + \Re[{}^1\underline{\hat{w}}(x, y, z)\mathrm{e}^{\mathrm{i}2\pi f t}] \\
\underline{w}_{(2)}(x, y, z, t) &= {}^0\underline{w}(x, y, z) + \Re[{}^2\underline{\hat{w}}(x, y, z)\mathrm{e}^{\mathrm{i}2\pi 2 f t}] \\
\underline{w}_{(3)}(x, y, z, t) &= {}^0\underline{w}(x, y, z) + \Re[{}^3\underline{\hat{w}}(x, y, z)\mathrm{e}^{\mathrm{i}2\pi 3 f t}]
\end{aligned} \tag{20}$$

3.3. Unsteady flow results

3.3.1. Comparison with measurements and time-nonlinear computations. Time-linearized time-harmonic computational results are compared with previous time-nonlinear computations [72] and

DOI: 10.1002/fld

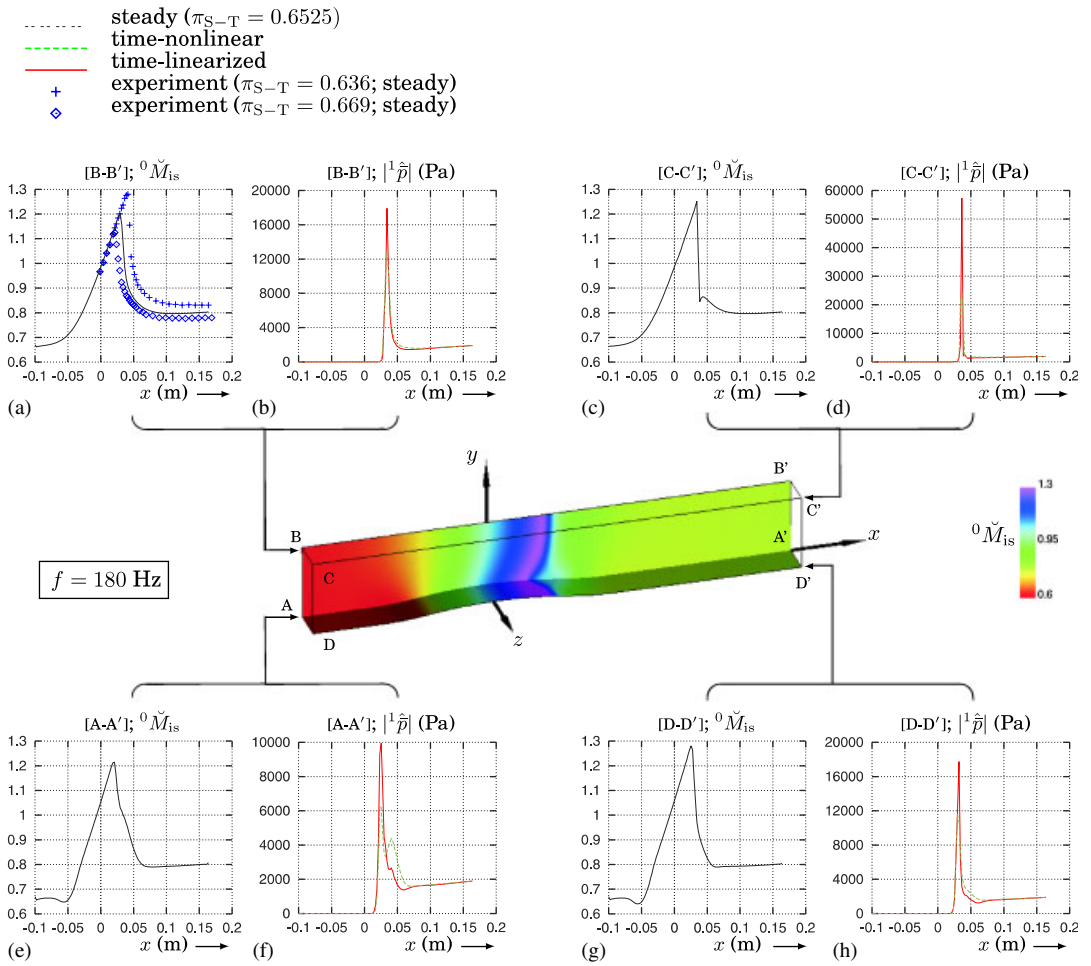

Figure 2. Steady RSM–RANS computation [66] x-wise distributions of wall-isentropic-Mach-number ${}^0\breve{M}_{is}$ and comparison of time-linearized time-harmonic computations for $f = 180$ Hz (x-wise distributions of $|{}^1\hat{\tilde{p}}|$) with time-nonlinear RSM–RANS computations [72] at the corner-lines of the computational domain of the Ott *et al.* [82] nozzle (grid_A [72]).

with measurements [81, 82] (Figures 1–3). The present time-linearized scheme is obtained by the linearization of the previously used time-nonlinear method [72], the only difference being that the RSM-transport equations were not linearized, but were replaced by the frozen-turbulence-scales assumption instead (cf. Appendix A). Therefore, eventual differences between the time-nonlinear and the time-linearized results can be attributed to either the linearization itself, or to the fact that the turbulence transport equations were not linearized.

For a back-pressure fluctuation-frequency $f = 180$ Hz, corresponding to a Strouhal number $Sr_\chi = f\chi/u_i = 0.192$ (where $\chi = 133$ mm is the nozzle bump length, u_i is the inflow velocity), the computed x-wise distribution of ${}^1\hat{\tilde{p}}$ is in very good agreement with both measurements [81, 82]

DOI: 10.1002/fld

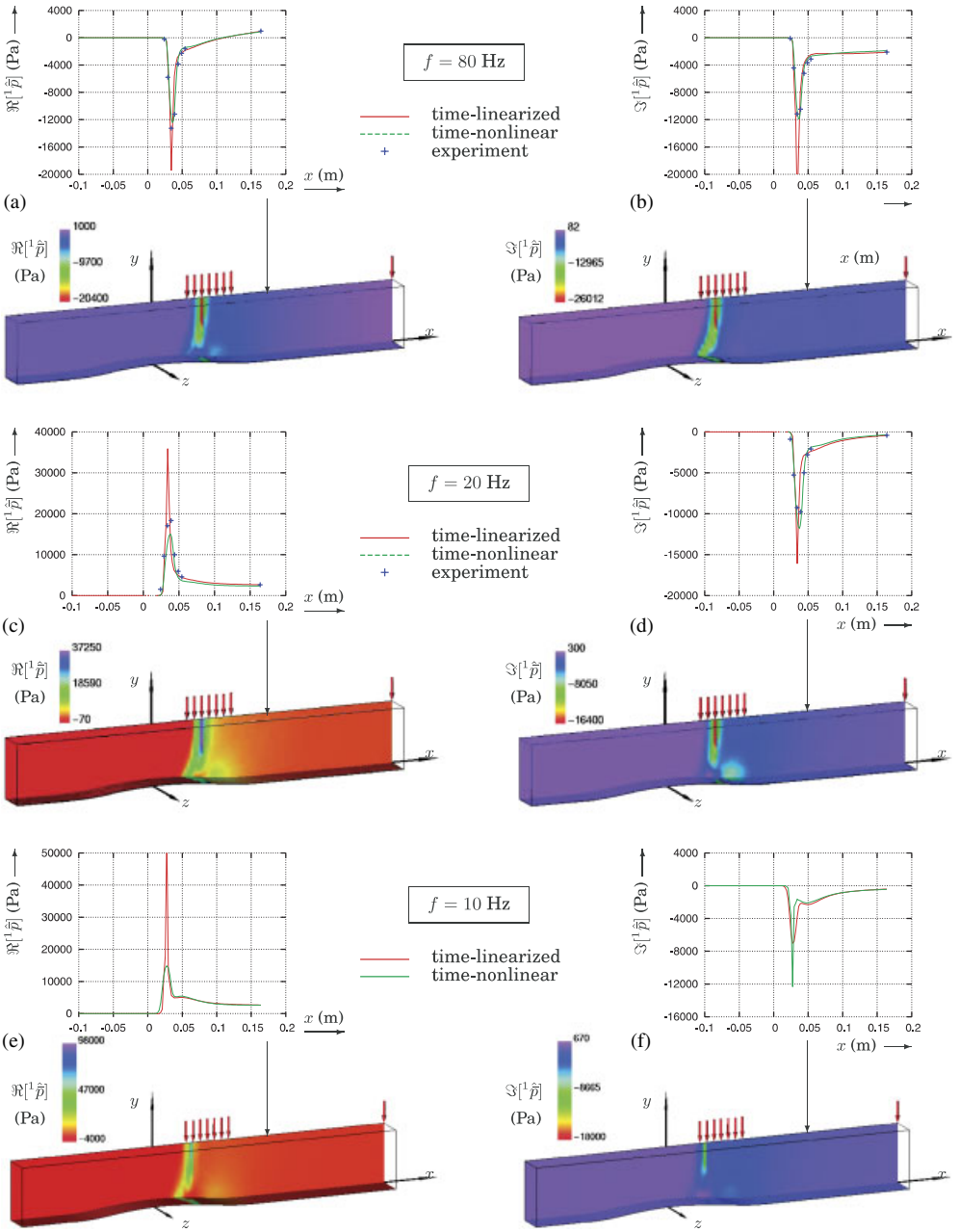

Figure 3. Comparison of time-linearized time-harmonic computations for $f = 10, 20$ and $80\,\mathrm{Hz}$ (x-wise distributions and wall-levels of $\Re[{}^1\hat{p}]$ and $\Im[{}^1\hat{p}]$) with measurements [81, 82] (pressure probes indicated by the solid red arrows) and with time-nonlinear RSM–RANS computations [72] for the Ott *et al.* [82] nozzle (grid_A [72]; notice that the plot-ranges are automatic and that measurements were not available for $f = 10\,\mathrm{Hz}$).

DOI: 10.1002/fld

and time-nonlinear [72] results (Figure 1(a)–(c)), both in amplitude and phase. The peak of $|^1\hat{\tilde{p}}|$ at the shock-wave predicted by the time-linearized computations is systematically higher than in the time-nonlinear predictions (Figure 1(a)), corroborating previous results [22, 57] suggesting that the time-linearized method corresponds to the limit of vanishing amplitude of the time-nonlinear scheme (scaled by the back-pressure amplitude). The x-wise distributions of $^2\hat{\tilde{p}}$ are correctly predicted (Figure 1(d)–(f)), except at the shock-wave location, especially for the real and imaginary part (Figure 1(e) and (f)), where nonlinearities are important (the time-nonlinear computations were run for the complete back-pressure-signal, so that they include the nonlinear interactions between harmonics, contrary to the time-linearized method). The same remarks hold for $^3\hat{\tilde{p}}$ (Figure 1(g)– (i)), although the amplitude is not correctly predicted, even in the nonlinear computations, probably because of insufficient grid-resolution, but also because the amplitude decreases with increasing harmonic number m (Figure 1(j); notice that the scale of the plots is different for different harmonics).

Quite satisfactory agreement is observed in the x-wise distributions of $|^1\hat{\tilde{p}}|$ at the corner-lines of the computational domain (Figure 2), between the time-linearized and the time-nonlinear computations. Nevertheless, discrepancies are observed at the shock-wave location, on the solid corner-line at the intersection between the lower-wall and the sidewall (Figure 2(f)). The failure of the time-linearized approach to correctly reproduce the second $|^1\hat{\tilde{p}}|$-peak (Figure 2(f)) is attributed to the complex phenomena related to the corner recirculation bubble, combining nonlinear effects and high turbulence levels [82] (the complete linearization of the RSM-transport equations might improve the agreement with the time-nonlinear results).

Examination of the results for back-pressure fluctuation-frequencies $f = 10\,\text{Hz}$ ($Sr_\chi = 0.006$), $f = 20\,\text{Hz}$ ($Sr_\chi = 0.0121$) and $f = 80\,\text{Hz}$ ($Sr_\chi = 0.0485$) yields similar conclusions as for $f =$ 180 Hz (Figure 3). For all of the frequencies studied (Figures 1, 3), the imposed pressure-fluctuation propagation up to the shock-wave, and the amplitude-peak produced by their interaction, are quite well predicted, both by the time-linearized and by the time-nonlinear computations. As the flow upstream of the shock-wave is supersonic, there is no noticeable pressure-disturbance propagating further upstream (Figures 1 and 3). The computation at $f = 10$ Hz ($Sr_\chi = 0.006$), for which no experimental data were available, was included as a comparison between the time-linearized and the time-nonlinear methods, because it was observed that the discrepancy between the time-linearized and the time-nonlinear results increases as f decreases from 180 to 20 Hz (Figures 1–3). In the absence of experimental data, the same back-pressure-signal was used for $f = 10\,\text{Hz}$ as for $f = 20\,\text{Hz}$ (Table II). With this same outflow-pressure forcing, the difference between the time-linearized and the time-nonlinear results increases (Figure 3). This is attributed to the fact that, for a given back-pressure fluctuation amplitude, the shock-wave excursion becomes larger as the frequency decreases, so that the pressure-amplitude peak at the shock-wave foot becomes larger and less sharp, while the time-linearized computation cannot reproduce this effect (it reproduces the pressure-fluctuations corresponding to the limit of negligibly small amplitudes, and correctly predicts the pressure-integrals, i.e. the global forces, but not the flow details in the vicinity of the shock-wave).

3.3.2. Grid refinement study. Grid-convergence of the time-linearized computations was studied (for $f = 180\,\text{Hz}$), by refining the original 0.34×10^6 points grid ($121 \times 57 \times 49$ grid_A [72]) either in the x-wise direction only (0.56×10^6 points $201 \times 57 \times 49$ grid_B [72]) or in all three directions (2.03×10^6 points $201 \times 111 \times 91$ grid_C [72]). Comparison of x-wise distributions of

DOI: 10.1002/fld

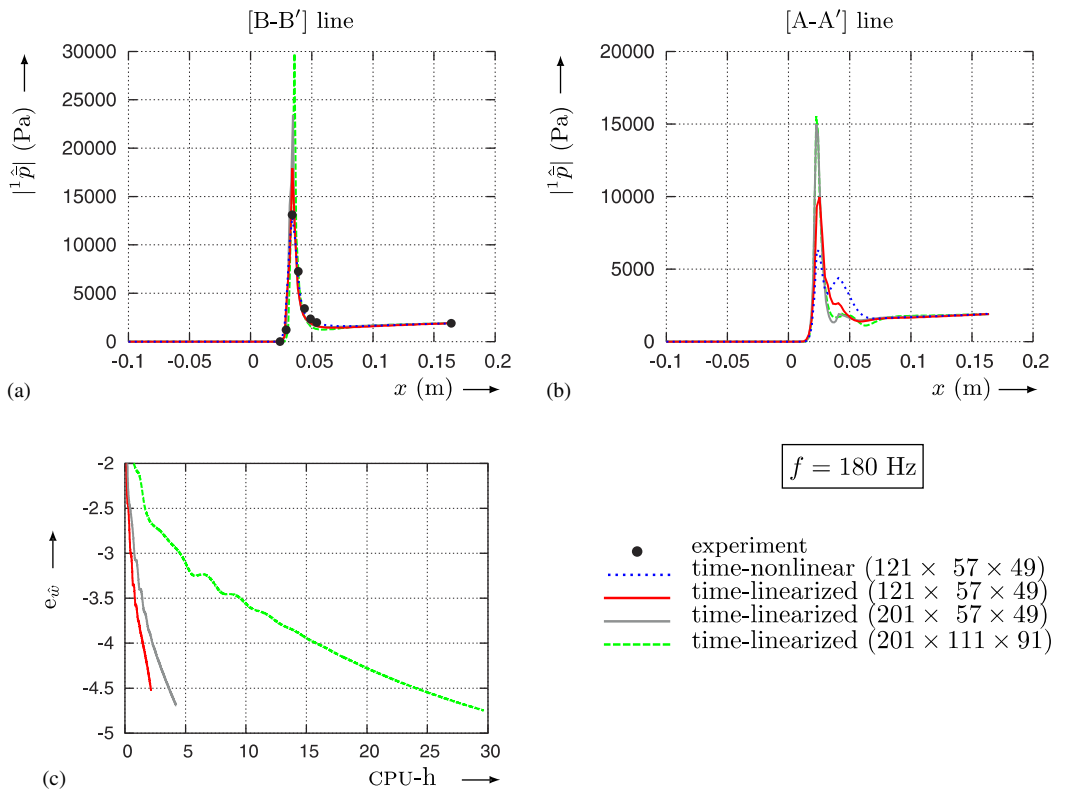

Figure 4. Convergence-histories (c; $e_{\hat{w}}$ *vs* CPU-h, for 2 Gflops sustained performance) of time-linearized time-harmonic computations using three different grids [72] ($121 \times 57 \times 49$ grid_A, $201 \times 57 \times 49$ grid_B, and $201 \times 111 \times 91$ grid_C) for $f = 180$ Hz, and comparison (a, b) of computed x-wise distributions of $|^1\hat{\tilde{p}}|$ at the intersection between the sidewall and the y-symmetry plane (line $[B - B']$ in Figure 2) and at the solid corner (line $[A - A']$ in Figure 2) with measurements [81, 82] and with time-nonlinear RSM–RANS computations [72] (grid_A [72]) for the Ott *et al.* [82] nozzle.

$|^1\hat{\tilde{p}}|$ at the experimental pressure-transducers location (Figure 4(a)) shows how the amplitude-peak at the shock-wave becomes higher and narrower, as the grid is refined in the x-wise direction (cf. Lindquist and Giles [22]). The same behaviour is observed at the solid corner (Figure 4b).

The convergence of the computations is monitored by the error-$L2$-norm (Figure 4(c))

$$e_{\hat{w}} = \log_{10}\left(\frac{\|^{(n+1)}[^1\hat{\mathbf{w}}] - {}^{(n)}[^1\hat{\mathbf{w}}]\|_2}{\|^{(n)}[^1\hat{\mathbf{w}}]\|_2}\right) \tag{21}$$

The computational time required for a reduction by three orders-of-magnitude of the residuals (Figure 4(c)) is 2 CPU-h for grid_A, 2.5 CPU-h for grid_B and 15 CPU-h for grid_C (~ 2 Gflops sustained performance).

3.3.3. Pressure-integral per unit amplitude. As explained by Lindquist and Giles [22], for flows with shock-waves, the shock-capturing time-linearized analysis correctly predicts the shock-loads at

DOI: 10.1002/fld

Table III. Comparison of wall-pressure-loads between the time-linearized (TL) and the time-nonlinear (TNL) methods for various grids ($N_i \times N_j \times N_k$) and back-pressure fluctuation-frequencies.

Frequency	180 Hz			80 Hz	20 Hz	10 Hz
Grid	$121 \times 57 \times 49$	$201 \times 57 \times 49$	$201 \times 111 \times 91$	$121 \times 57 \times 49$	$121 \times 57 \times 49$	$121 \times 57 \times 49$
$\lvert{}^1\hat{C}_y\rvert$ TNL	0.6677	0.6698	—	0.8482	0.9149	0.9879
$\lvert{}^1\hat{C}_y\rvert$ TL	0.6394	0.6683	0.6598	0.8462	0.9804	1.0403
$\lvert{}^1\hat{C}_z\rvert$ TNL	0.6654	0.6698	—	0.8475	0.9119	0.9893
$\lvert{}^1\hat{C}_z\rvert$ TL	0.6384	0.6609	0.6528	0.8594	0.9822	1.0478

the wall (for small amplitudes), but not the exact details of the shock-wave motion. This capability makes the time-linearized shock-capturing analysis suitable for providing unsteady aerodynamic response information such as aerodynamic damping. It is therefore important to examine the unsteady loads on the solid walls

$$ {}^1\hat{C}_y = \left[\int_0^1 \int_0^1 \frac{{}^1\hat{\tilde{p}}(x, y, z)}{|{}^1\hat{\tilde{p}}_o|} \mathrm{d}\left(\frac{x - x_i}{x_o - x_i}\right) \mathrm{d}\left(\frac{y - y_i}{y_o - y_i}\right) \right]_{z=0} \tag{22} $$

$$ {}^1\hat{C}_z = \left[\int_0^1 \int_0^1 \frac{{}^1\hat{\tilde{p}}(x, y, z)}{|{}^1\hat{\tilde{p}}_o|} \mathrm{d}\left(\frac{x - x_i}{x_o - x_i}\right) \mathrm{d}\left(\frac{z - z_i}{z_o - z_i}\right) \right]_{y=0} \tag{23} $$

where ${}^1\hat{C}_y$ and ${}^1\hat{C}_z$ denote the 1-harmonic pressure-loads on the walls perpendicular to y and z respectively, $|{}^1\hat{\tilde{p}}_o|$ is the amplitude of the 1-harmonic of pressure at outflow, and the subscripts i and o denote values at inflow and outflow, respectively.

Comparison of time-linearized and time-nonlinear results, for $f = 10, 20, 80, 180$ Hz on various computational grids (Table III), shows very good agreement between the two methods and between various computational grids (differences less than 2%), with the exception of the lower frequencies ($f = 10, 20$ Hz), for which nonlinear effects appear to be more pronounced (differences of $\sim 7\%$; Table III).

3.3.4. Computational-time requirements. The main interest in the use of time-linearized methods for unsteady aerodynamics is the potential gain in computing-time [18, 29]. The corresponding time-nonlinear method considered in the present work [72], is based on a very efficient dual-time-stepping technique with implicit subiterations, in which the number of instants-per-period is fixed by the user, and the number of subiterations is dynamically adjusted at each iteration to attain a given increment-convergence-tolerance r_{MF}. For the present problem, the simulation of $N_{\mathrm{P}} \in [3, 4]$ periods, with $N_{\mathrm{PP}} = 360$ instants-per-period (requiring $M_{\mathrm{it}} \in [10, 30]$ subiterations per iteration with $r_{\mathrm{MF}} = -1.5$), is sufficient for achieving periodic convergence with the time-nonlinear solver [72]. Because N_{PP} is user-defined, and independent of the fluctuation frequency (Table IV), the computational-time of the time-nonlinear method does not scale as f^{-1}, but increases much slower as $f \longrightarrow 0$ (Table IV). This is therefore a rather stringent test for the performance of the time-linearized method (notice that for different test cases, such as compressor-blade flutter [4] or rotor/stator interaction [85], a much higher number of periods must be simulated to reach periodic convergence). In comparing computing times (Table IV), $N_{\mathrm{P}} \in [3, 4]$ (as applicable to

DOI: 10.1002/fld

Table IV. Computational-time requirements of the time-linearized and the time-nonlinear solvers (2 Gflops sustained performance).

Computation	Grid ($N_i \times N_j \times N_k$)	Frequency (Hz)	CPU-cost (s/it)	Iterations	CPU-time (h)	Memory (Mb)
Time-nonlinear	$121 \times 57 \times 49$	180	36	3×360	10.8	685
Time-nonlinear	$121 \times 57 \times 49$	80	39	3×360	11.4	685
Time-nonlinear	$121 \times 57 \times 49$	20	55	3×360	16.5	685
Time-nonlinear	$121 \times 57 \times 49$	10	66	4×360	26.3	685
Time-nonlinear	$201 \times 57 \times 49$	180	57	3×360	17.1	980
Time-linearized	$121 \times 57 \times 49$	180	2.6	2500	1.8	416
Time-linearized	$121 \times 57 \times 49$	80	2.5	2500	1.8	416
Time-linearized	$121 \times 57 \times 49$	20	2.6	2500	1.9	416
Time-linearized	$121 \times 57 \times 49$	10	2.6	2500	1.9	416
Time-linearized	$201 \times 57 \times 49$	180	4.2	2500	2.9	656
Time-linearized	$201 \times 101 \times 91$	180	15.5	3500	15.1	2256

obtain periodic convergence of results) was used for the time-nonlinear computations, while the time-linearized calculations were run until convergence of the wall-pressure-loads (Equations (22, 23)). Notice that for the time-nonlinear computations, for the $f = 10$ Hz case, the simulation of one more period ($N_P = 4$ instead of $N_P = 3$) was necessary to achieve convergence of the unsteady signals, while the convergence of the corresponding time-linearized computations was not significantly influenced by the change in frequency. An average speed-up of ~ 10 is obtained using the time-linearized method.

4. STABILITY AND ROBUSTNESS

Refining the computational grid in recirculating flow regions (shock-wave/corner-boundary-layers interaction region), using the pseudo-time-marching integration technique, may lead to instability of the iterative procedure, with the perturbation variables growing continuously in pseudo-time. This is associated with the pseudo-time-marching iterative technique used (cf. Section 2.6). In a recent paper, Agarwal *et al.* [54] have shown that the linearized Euler equations contain instabilities associated with a given range of frequencies, depending on the unperturbed (time-averaged) flow. These instabilities will be reproduced in the pseudo-time-marching procedure. These authors [54] have in particular shown that these instabilities will not contaminate the solution if a direct (not pseudo-time-marching) solver is used. This has been verified using a 2-D version of the present method, with direct unfactored LU inversion of the linear system (which does not present instability problems, in agreement with the results of Rao and Morris [36]).

As work on time-linearized approaches focuses on the prediction of unsteady flows with strong viscous effects (separated flows) [24, 29, 31, 42, 58, 61], encounters with instability become more frequent. For a given configuration, the appearance of instability depends on the grid refinement [59], on the dissipative properties of the scheme [59], or on the time-linearization of the turbulence model [42]. For a given configuration which contains unstable modes, numerical instability is enhanced as the grid is refined [59], as the numerical dissipation decreases [59], or when the unsteady behaviour of turbulence is neglected [42].

DOI: 10.1002/fld

Campobasso and Giles [34, 35] have demonstrated the presence of unstable modes in the linearized Navier–Stokes equations, and have developed an implicit pseudo-time-marching technique where the pseudo-time-advancement linear system solution, at each pseudo-time iteration, is based on a GMRES [41, 46] approach or on a RPM [47] procedure to filter out the transient iterative instabilities.

A different approach, which has been successfully applied to the stabilization of the computation of a 2-D transonic nozzle flow response to a pressure impulse imposed at outflow [55], is to solve the linear system using a non-time-marching restarted-GMRES [41] procedure. The instability problem encountered in Chassaing *et al.* [55], appeared for the Délery_B nozzle [86], computed with the GV-RSM [68], on a 301×201 grid. The restarted-GMRES, with ILU0 preconditioning [41], used a basis of 400 (800) vectors with 12 (2) restarts. This methodology should be preferred for robustness, instead of the time-marching methods used in the present work.

5. CONCLUSIONS

In the present work an upwind finite-volume numerical method with shock-capturing capability was developed for the time-linearized time-harmonic Reynolds-averaged Navier–Stokes equations. The convective numerical fluxes are obtained from the linearization of the nonlinear van Leer flux-vector-splitting scheme. A conservative variables reconstruction technique with frozen slope limiters (computed using the underlying steady flow only) is used to achieve $O(\Delta x_{\mathrm{H}}^3)$ accuracy. A straightforward linearization of the viscous fluxes, with an $O(\Delta x_{\mathrm{H}}^2)$ centred scheme is used. A very simple frozen-turbulence-scales assumption was used for the unsteady turbulent stresses (the underlying steady flow is obtained using an RSM closure) as a baseline model to validate the numerical method.

The solution of the resulting linear system is obtained using an implicit pseudo-time-marching technique with ADI-AF factorization. When the underlying steady flow contains unstable modes, the pseudo-time-marching technique may develop numerical instabilities. This problem is best solved by using non-pseudo-time-marching techniques to solve the linear system (this is the subject of ongoing research).

Time-linearized results are compared with experimental measurements and with time-nonlinear computations for a transonic nozzle, in which back-pressure fluctuation induces the oscillation of the 3-D shock-wave present in the divergent section of the nozzle, for frequencies $f \in [10, 180]$ Hz. The agreement between time-nonlinear, time-linearized and experimental results is quite satisfactory. Discrepancies are observed locally at the shock-wave, where nonlinear interactions between harmonics (present in the experiment and simulated by the time-nonlinear method) cannot be taken into account by the time-linearized method. The time-linearized method also fails to reproduce the double shock-wave amplitude-peak, observed in the time-nonlinear results, at the solid corner between the lower-wall and the sidewall. This is attributed to the very simple assumption used for the unsteady part of the turbulent stresses, and to the nonlinearities associated with the complex secondary flows present at this location. Most importantly, the time-linearized method accurately predicts the aerodynamic loads on the solid walls, being faster by a factor ~ 10 compared to the time-nonlinear solver.

Future work on the time-linearized method should concentrate (1) on the use of non-pseudo-time-marching solvers of the nonlinear system (suppression of numerical instabilities associated with the pseudo-time-marching technique), (2) on the multigrid convergence acceleration of the

DOI: 10.1002/fld

time-linearized computations, and (3) on the linearization of the RSM-transport equations to improve upon the present oversimplified frozen-turbulence assumption, especially in regions with strong secondary flows.

APPENDIX A: SIMPLIFIED PERTURBATIONS OF TURBULENT STRESSES AND HEAT-FLUXES

The thermodynamics of the working gas are approximated by [68]

$$\begin{aligned} &\bar{p} = \bar{\rho} R_{\mathrm{g}} \tilde{T} = \bar{\rho} \frac{\gamma - 1}{\gamma} \tilde{h}, \quad \breve{\mu} = \mu(\tilde{T}) = \mu_{273} \frac{\tilde{T}^{3/2}}{273.15^{3/2}} \frac{T_S + 273.15}{T_S + \tilde{T}} \\ &\breve{\kappa} = \kappa(\tilde{T}) = \kappa_{273} \frac{\mu(\tilde{T})}{\mu_{273}} [1 + A_\kappa (\tilde{T} - 273.15)] \end{aligned} \tag{A1}$$

where γ is the isentropic exponent, R_{g} is the gas-constant, μ is the dynamic viscosity, and κ is the heat conductivity. For air R_{g}=287.04 $\mathrm{m^2\,s^{-2}\,K^{-1}}$, γ=1.4, μ_{273}=17.11$\times 10^{-6}$ Pa s, κ_{273}= 0.0242 $\mathrm{W\,m^{-1}\,K^{-1}}$, $T_S = 110.4$ K, and $A_\kappa = 0.00023\,\mathrm{K^{-1}}$.

The unsteady perturbations of the viscous fluxes and of the source-terms, for the meanflow-variables equations, read

$${}^1\hat{\underline{F}}^{\mathrm{V}}_{\mathrm{MF}_\ell} = \begin{bmatrix} 0 \\ -{}^1\hat{\bar{\tau}}_{x\ell} + {}^1\hat{\bar{\tau}}_{uu_\ell} \\ -{}^1\hat{\bar{\tau}}_{y\ell} + {}^1\hat{\bar{\tau}}_{vu_\ell} \\ -{}^1\hat{\bar{\tau}}_{z\ell} + {}^1\hat{\bar{\tau}}_{wu_\ell} \\ -{}^0u_i({}^1\hat{\bar{\tau}}_{i\ell} - {}^1\hat{\bar{\tau}}_{u_iu_\ell}) - {}^1\hat{u}_i({}^0\bar{\tau}_{i\ell} - {}^0\bar{\tau}_{u_iu_\ell}) + ({}^1\hat{q}_\ell + {}^1\hat{q}_{hu_\ell}) \end{bmatrix}, \quad {}^1\hat{\underline{S}}_{\mathrm{MF}} = \begin{bmatrix} 0 \\ 0 \\ 0 \\ 0 \\ -{}^1\hat{\underline{S}}_{\breve{h}_t} \end{bmatrix} \tag{A2}$$

where $\hat{\underline{F}}^{\mathrm{V}}_{\mathrm{MF}_\ell} \in \mathbb{R}^5$ are the viscous fluxes in the mean-flow equations, $\hat{\underline{S}}_{\mathrm{MF}}$ are the source-terms in the mean-flow equations, $\bar{\tau}_{ij}$ are the viscous stresses, $\bar{\tau}_{u_iu_j} = \bar{\rho}\widetilde{u_i''u_j''}$ are the Reynolds-stresses, $\bar{q}_i$ is the molecular heat-flux, $\bar{q}_{hu_i} = \bar{\rho}\widetilde{h''u_i''}$ is the turbulent heat-flux, $S_{\breve{h}_t} = -(P_k - \bar{\rho}\varepsilon + \overline{p'\partial u_\ell''/\partial x_\ell}) + \partial[\overline{pu_\ell''}]/\partial x_\ell + (-\bar{p}\delta_{i\ell} + \bar{\tau}_{i\ell})\partial\overline{u_i''}/\partial x_\ell$ is the source term in the mean-flow energy-equation [68], $P_{\mathrm{k}} = \frac{1}{2}P_{\ell\ell}$ is the turbulence kinetic energy production (equal to the trace of the Reynolds-stresses production tensor P_{ij}), and ε its dissipation. Notice that in the last member of the vector ${}^1\hat{\underline{F}}^{\mathrm{V}}_{\mathrm{MF}_\ell}$ (Equation (A2)) the summation convention is observed on the index i (e.g. ${}^1\hat{\bar{u}}_i{}^0\bar{\tau}_{i\ell} = {}^1\hat{\bar{u}}{}^0\bar{\tau}_{x\ell} + {}^1\hat{\bar{v}}{}^0\bar{\tau}_{x\ell} + {}^1\hat{\bar{w}}{}^0\bar{\tau}_{x\ell}$). The harmonics of the primitive variables $\underline{v}$ are directly related to the harmonics of the conservative variables

$${}^1\hat{\underline{v}} = \left[\frac{\partial \underline{v}}{\partial \underline{w}}({}^0\underline{v})\right] {}^1\hat{\underline{w}}, \quad \underline{v} = [\bar{\rho}, \tilde{u}, \tilde{v}, \tilde{w}, \bar{p}]^{\mathrm{T}} \tag{A3}$$

where the Jacobian matrix $\partial\underline{v}/\partial\underline{w}$ is given, e.g. in Warming *et al.* [87].

DOI: 10.1002/fld

The unsteady perturbations of the Reynolds-stresses and of the turbulent-heat-flux are modelled using only steady quantities and mean-flow-perturbations

$$ {}^1\hat{\tau}_{u_iu_j} = {}^1\hat{\tau}_{u_iu_j}({}^0\underline{w}, \text{grad}\,{}^0\underline{w}, {}^1\underline{\hat{w}}_{\text{MF}}, \text{grad}\,{}^1\underline{\hat{w}}_{\text{MF}}) \tag{A4} $$

$$ {}^1\hat{q}_{hu_i} = {}^1\hat{q}_{hu_i}({}^0\underline{w}, \text{grad}\,{}^0\underline{w}, {}^1\underline{\hat{w}}_{\text{MF}}, \text{grad}\,{}^1\underline{\hat{w}}_{\text{MF}}) \tag{A5} $$

These assumptions require a specific approximation for the unsteady perturbations of the Reynolds-stresses, which is not consistent with the linearization of the transport-equations used in the steady flow model (Equation (1)). In the present work, we have used a very simple approximation, in which (1) a Boussinesq tensorial relation [63] for the unsteady perturbations of the Reynolds-stresses is used, (2) the unsteady perturbations of the turbulent kinetic-energy $k = \frac{1}{2}\widetilde{u_i'' u_i''}$ and of the turbulence Reynolds-number $Re_{\text{T}}^* = k^2 \breve{\nu}^{-1} \varepsilon^{*^{-1}}$ are neglected, and (3) the unsteady perturbations of the source-term in the energy equation are neglected

$$ {}^1\hat{k} \cong 0, \quad {}^1\hat{Re}_{\text{T}}^* \cong 0, \quad {}^1\underline{\hat{S}}_{\breve{h}_t} \cong 0 \tag{A6} $$

With these assumptions, the unsteady perturbations of the equivalent (molecular + turbulent) stresses and heat-fluxes read

$$ \begin{aligned} {}^1\hat{\tilde{\tau}}_{ij} - {}^1\hat{\tau}_{u_iu_j} = ({}^1\hat{\breve{\mu}} + {}^1\hat{\mu}_{\text{T}}) \left(\frac{\partial\, {}^0\tilde{u}_i}{\partial x_j} + \frac{\partial\, {}^0\tilde{u}_j}{\partial x_i} - \frac{2}{3}\frac{\partial\, {}^0\tilde{u}_\ell}{\partial x_\ell}\delta_{ij} \right) \\ + ({}^0\breve{\mu} + {}^0\mu_{\text{T}}) \left(\frac{\partial\, {}^1\hat{\tilde{u}}_i}{\partial x_j} + \frac{\partial\, {}^1\hat{\tilde{u}}_j}{\partial x_i} - \frac{2}{3}\frac{\partial\, {}^1\hat{\tilde{u}}_\ell}{\partial x_\ell}\delta_{ij} \right) - \frac{2}{3}\, {}^1\hat{\bar{\rho}}\, {}^0k \end{aligned} \tag{A7} $$

$$ {}^1\hat{\tilde{q}}_i + {}^1\hat{\tilde{q}}_{hu_i} = -({}^0\kappa + {}^0\kappa_{\text{T}})\frac{\partial\, {}^1\hat{\tilde{T}}}{\partial x_i} - ({}^1\hat{\kappa} + {}^1\hat{\kappa}_{\text{T}})\frac{\partial\, {}^0\tilde{T}}{\partial x_i} \tag{A8} $$

with

$$ {}^0\mu_{\text{T}} = {}^0C_\mu\, {}^0\breve{\mu}\, {}^0Re_{\text{T}}^*, \quad {}^0C_\mu = 0.09\text{e}^{-3.4/(1+0.02\,{}^0Re_{\text{T}}^*)^2}, \quad {}^0Re_{\text{T}}^* = \frac{{}^0\bar{\rho}\, {}^0k^2}{{}^0\breve{\mu}\, {}^0\varepsilon^*} \tag{A9} $$

$$ {}^1\hat{\mu}_{\text{T}} = {}^0C_\mu\, {}^0Re_{\text{T}}^*\, {}^1\hat{\breve{\mu}}, \quad {}^0\kappa_{\text{T}} = \frac{{}^0\mu_{\text{T}} c_p}{Pr_{\text{T}}}, \quad {}^1\hat{\kappa}_{\text{T}} = \frac{c_p}{Pr_{\text{T}}}\, {}^1\hat{\mu}_{\text{T}}, \quad c_p = \frac{\gamma}{\gamma - 1}R_{\text{g}} \tag{A10} $$

where c_p is the heat capacity at constant pressure, and Pr_{T} is the turbulent Prandtl number (for air $Pr_{\text{T}} = 0.9$ is used to obtain the correct recovery temperature for turbulent flow over an adiabatic wall [88]). The unsteady perturbations of $\breve{\mu}$ and $\breve{\kappa}$ are obtained by straightforward differentiation of Equation (A1)

$$ {}^1\hat{\breve{\mu}} = {}^0\breve{\mu}\left(\frac{3}{2\,{}^0\tilde{T}} - \frac{1}{T_S + {}^0\tilde{T}} \right) {}^1\hat{\tilde{T}}, \quad {}^1\hat{\breve{\kappa}} = \frac{{}^0\breve{\kappa}}{{}^0\breve{\mu}}\, {}^1\hat{\breve{\mu}} + \frac{\kappa_{273}}{\mu_{273}}\, {}^0\breve{\mu} A_\kappa\, {}^1\hat{\tilde{T}} \tag{A11} $$

Space-derivatives (Equations (A2), (A4), (A5), (A7) and (A8)) are computed using an $O(\Delta x_{\text{H}}^2)$ discretization [73].

DOI: 10.1002/fld

Obviously, this oversimplified frozen-turbulence-scales approximation should be considered as a baseline model used to test the numerical methodology, and further research on a physically representative 0-equation model for the unsteady perturbations of the Reynolds-stresses is needed.

APPENDIX B: MUSCL INTERPOLATION

If w_p is an element of $\underline{w}_{\mathrm{MF}} = [w_p;\ p = 1, \ldots, 5]^{\mathrm{T}}$ then the elements of the corresponding van Albada limiter $\underline{s}_{\mathrm{MF}} = [s_p;\ p = 1, \ldots, 5]^{\mathrm{T}}$ are defined by [48]

$$s_p([w_p]_{-1}, [w_p]_0, [w_p]_{+1}) = \frac{2([w_p]_{+1} - [w_p]_0)\ ([w_p]_0 - [w_p]_{-1}) + 10^{-23}}{([w_p]_{+1} - [w_p]_0)^2 + ([w_p]_0 - [w_p]_{-1})^2 + 10^{-23}}, \quad p=1, \ldots, 5 \tag{B1}$$

where the 10^{-23} term is introduced to avoid division by 0, and the elements of the corresponding MUSCL interpolation function

$$\underline{\mathrm{w}}^{\pm}_{\mathrm{MF}}([\underline{w}_{\mathrm{MF}}]_{-1}, [\underline{w}_{\mathrm{MF}}]_0, [\underline{w}_{\mathrm{MF}}]_{+1}; \underline{s}_{\mathrm{MF}}) = [\mathrm{w}^{\pm}_p;\ p = 1, \ldots, 5]^{\mathrm{T}} \tag{B2}$$

are given by [48]

$$\mathrm{w}^{\pm}_p([w_p]_{-1}, [w_p]_0, [w_p]_{+1}) = [w_p]_0 \mp \left[\frac{s_p}{4}\left(1 \mp \frac{s_p}{3}\right)([w_p]_{+1} - [w_p]_0) + \frac{s_p}{4}\left(1 \pm \frac{s_p}{3}\right)([w_p]_0 - [w_p]_{-1})\right] \tag{B3}$$

Using the above symbolism, and neglecting the unsteady perturbations of the limiter $\underline{s}_{\mathrm{MF}}$ the unsteady perturbations of the MUSCL variables are given by

$$\begin{aligned}
[{}^1\hat{\underline{w}}^{\pm}_{\mathrm{MF}}]_{i-1/2,j,k} &= \underline{\mathrm{w}}^{\pm}_{\mathrm{MF}}([{}^1\hat{\underline{w}}_{\mathrm{MF}}]_{i-3/2\pm1/2,j,k}, [{}^1\hat{\underline{w}}_{\mathrm{MF}}]_{i-1/2\pm1/2,j,k}, [{}^1\hat{\underline{w}}_{\mathrm{MF}}]_{i+1/2\pm1/2,j,k}; {}^0\underline{s}_{\mathrm{MF}}) \\
[{}^1\hat{\underline{w}}^{\pm}_{\mathrm{MF}}]_{i,j-1/2,k} &= \underline{\mathrm{w}}^{\pm}_{\mathrm{MF}}([{}^1\hat{\underline{w}}_{\mathrm{MF}}]_{i,j-3/2\pm1/2,k}, [{}^1\hat{\underline{w}}_{\mathrm{MF}}]_{i,j-1/2\pm1/2,k}, [{}^1\hat{\underline{w}}_{\mathrm{MF}}]_{i,j+1/2\pm1/2,k}; {}^0\underline{s}_{\mathrm{MF}}) \\
[{}^1\hat{\underline{w}}^{\pm}_{\mathrm{MF}}]_{i,j,k-1/2} &= \underline{\mathrm{w}}^{\pm}_{\mathrm{MF}}([{}^1\hat{\underline{w}}_{\mathrm{MF}}]_{i,j,k-3/2\pm1/2}, [{}^1\hat{\underline{w}}_{\mathrm{MF}}]_{i,j,k-1/2\pm1/2}, [{}^1\hat{\underline{w}}_{\mathrm{MF}}]_{i,j,k+1/2\pm1/2}; {}^0\underline{s}_{\mathrm{MF}})
\end{aligned} \tag{B4}$$

APPENDIX C: BOUNDARY CONDITIONS FOR THE NOZZLE PROBLEM

The computations presented in the present paper concern a transonic nozzle with fluctuating back-pressure. Because of the geometrical symmetry of the configuration, only $\frac{1}{4}$ of the nozzle was discretized (Figure 1). Let n denote the unit-normal at the boundary, with direction cosines $[n_x, n_y, n_z]^{\mathrm{T}}$. At the y-wise and z-wise symmetry planes symmetry conditions were applied

$$\frac{\partial\, {}^1\hat{\underline{w}}}{\partial n} = 0, \quad {}^1\hat{\tilde{u}}_i n_i = 0 \tag{C1}$$

DOI: 10.1002/fld

where n is the unit-normal to the symmetry-plane. Adiabatic wall conditions were applied at the solid walls

$$ {}^1\hat{\tilde{u}} = 0, \quad {}^1\hat{\tilde{v}} = 0, \quad {}^1\hat{\tilde{w}} = 0, \quad \frac{\partial\, {}^1\hat{\bar{p}}}{\partial n} = 0, \quad \frac{\partial\, {}^1\hat{\tilde{T}}}{\partial n} = 0 \tag{C2} $$

At outflow $(\cdot)_o$ the pressure harmonic is fixed at a given value ${}^1\hat{\bar{p}}_o$, and the other variables are extrapolated

$$ {}^1\hat{\bar{p}} = {}^1\hat{\bar{p}}_o, \quad \frac{\partial\, {}^1\bar{\rho}}{\partial n} = 0, \quad \frac{\partial\, {}^1\widehat{(\bar{\rho}\tilde{u})}}{\partial n} = 0, \quad \frac{\partial\, {}^1\widehat{(\bar{\rho}\tilde{v})}}{\partial n} = 0, \quad \frac{\partial\, {}^1\widehat{(\bar{\rho}\tilde{w})}}{\partial n} = 0 \tag{C3} $$

At the inflow-boundary, a linearized form of the 1-D nonreflecting condition of Hedstrom [89] is applied, which for the present case can be summarized as [90]

$$ \begin{gathered} {}^1\hat{\bar{p}} + {}^0\bar{\rho}\, {}^0a\, {}^1\hat{\tilde{u}} = 0, \quad {}^1\hat{\bar{p}} - {}^0a^2\, {}^1\hat{\bar{\rho}} = 0, \quad {}^1\hat{\tilde{v}} = 0 \\ {}^1\hat{\tilde{w}} = 0, \quad {}^1\hat{\bar{p}} - {}^0\bar{\rho}\, {}^0a\, {}^1\hat{\tilde{u}} = [{}^1\hat{\bar{p}}]^{\mathrm{SCH}} - {}^0\bar{\rho}\, {}^0a\, [{}^1\hat{\tilde{u}}]^{\mathrm{SCH}} \end{gathered} \tag{C4} $$

where the superscript $[\cdot]^{\mathrm{SCH}}$ denotes variables computed from the numerical scheme, prior to the application of boundary-conditions.

ACKNOWLEDGEMENTS

The computations presented in this work were run at the Institut pour le Développement des Ressources en Informatique Scientifique (IDRIS), where computer resources were made available by the Comité Scientifique. The authors are listed alphabetically.

REFERENCES

1. Verdon JM. Review of unsteady aerodynamic methods for turbomachinery aeroelastic and aeroacoustic applications. *AIAA Journal* 1993; **31**:235–250.
2. He L, Denton JD. Inviscid–viscous coupled solution of unsteady flows through vibrating blades: Part 1—description of the method. *ASME Journal of Turbomahinery* 1993; **115**:94–100.
3. He L, Denton JD. Inviscid–viscous coupled solution of unsteady flows through vibrating blades: Part 2—computational results. *ASME Journal of Turbomachinery* 1993; **115**:101–109.
4. Gerolymos GA. Advances in the numerical integration of the 3-D Euler equations in vibrating cascades. *ASME Journal of Turbomachinery* 1993; **115**:781–790.
5. Gerolymos GA. Coupled 3-D aeroelastic stability analysis of bladed disks. *ASME Journal of Turbomachinery* 1993; **115**:791–799.
6. Marshall JG, Imregun M. A review of aeroelasticity methods with emphasis on turbomachinery applications. *Journal of Fluids and Structures* 1996; **10**:237–267.
7. Vahdati M, Imregun M. A nonlinear aeroelasticity analysis of a fan blade using unstructured dynamic meshes. *Journal of Mechanical Engineering Science* 1996; **210**:549–564.
8. Gerolymos GA, Vallet I. Validation of 3-D Euler methods for vibrating cascade aerodynamics. *ASME Journal of Turbomachinery* 1996; **118**:771–782.
9. Sayma AI, Vahdati M, Imregun M, Green JS. Whole-assembly flutter analysis of a low-pressure turbine blade. *Aeronautical Journal* 1998; **102**:459–463.
10. Isomura K, Giles MB. A numerical study of flutter in a transonic fan. *ASME Journal of Turbomachinery* 1998; **120**:500–507.
11. Imregun M, Vahdati M. Aeroelasticity analysis of a bird-damaged fan assembly using a large numerical model. *Aeronautical Journal* 1999; **103**:569–578.

DOI: 10.1002/fld

12. Srivastava R, Bakhle MA, Keith Jr TG. Numerical simulation of aerodynamic damping for flutter analysis of turbomachinery blade-rows. *Journal of Propulsion and Power* 2003; **19**:260–267.
13. Srivastava R, Bakhle MA, Keith Jr TG, Stefko GL. Aeroelastic analysis of turbomachinery and: Part I—phase-lagged boundary-condition methods. *International Journal of Numerical Methods for Heat and Fluid Flow* 2004; **14**:366–381.
14. Srivastava R, Bakhle MA, Keith Jr TG, Hoyniak D. Aeroelastic analysis of turbomachinery: Part II—stability computations. *International Journal of Numerical Methods for Heat and Fluid Flow* 2004; **14**:382–402.
15. Sanders AJ, Hassan KK, Rabe DC. Experimental and numerical study of stall flutter in a transonic low-aspect ratio fan blisk. *ASME Journal of Turbomachinery* 2004; **126**:166–174.
16. Srivastava R, Keith Jr TG. Influence of shock-wave on turbomachinery blade-row flutter. *Journal of Propulsion and Power* 2005; **21**:167–174.
17. Ni RH, Sisto F. Numerical computation of nonstationary aerodynamics for flat plate cascades in compressible flow. *ASME Journal of Engineering for Power* 1976; **98**:165–170.
18. Hall KC, Crawley EF. Calculation of unsteady flows in turbomachinery using the linearized Euler equations. *AIAA Journal* 1989; **27**:777–787.
19. Hall KC, Lorence CB. Calculation of 3-D unsteady flows in turbomachinery using the linearized harmonic Euler equations. *ASME Journal of Turbomachinery* 1993; **115**:800–809.
20. Hall KC, Clark WS. Linearized Euler predictions of unsteady aerodynamic loads in cascades. *AIAA Journal* 1993; **31**:540–550.
21. Hall KC, Clark WS, Lorence CB. A linearized Euler analysis of unsteady transonic flows in turbomachinery. *ASME Journal of Turbomachinery* 1994; **116**:477–488.
22. Lindquist DR, Giles MB. Validity of linearized unsteady Euler equations with shock-capturing. *AIAA Journal* 1994; **32**:46–53 (also AIAA Paper 91-1598, 1991).
23. Ning W, He L. Computation of unsteady flows around oscillating blades using linear and nonlinear harmonic Euler methods. *ASME Journal of Turbomachinery* 1998; **120**:508–514.
24. He L, Ning W. Efficient approach for analysis of unsteady viscous flows in turbomachines. *AIAA Journal* 1998; **36**:2005–2012.
25. Sreenivas K, Witfield DL. Time- and frequency-domain numerical simulation of linearized Euler equations. *AIAA Journal* 1998; **36**:968–975.
26. Montgomery MD, Verdon JM. A 3-D linearized Euler analysis for blade rows. Part 1: aerodynamic and numerical formulations. In *Unsteady Aerodynamics*, *Aeroacoustics*, *and Aeroelasticity of Turbomachines—Proccedings of the 8th International Symposium*, *14–18 September 1997*, *Stockholm*, Fransson TH (ed.). Kluwer: Dordrecht, 1998; 211–224 (ISBN 0-7923-5040-5).
27. Montgomery MD, Verdon JM. A 3-D linearized Euler analysis for blade rows. Part 1: unsteady aerodynamic response predictions. In *Unsteady Aerodynamics, Aeroacoustics*, *and Aeroelasticity of Turbomachines—Proccedings of the 8th International Symposium*, *14–18 September 1997*, *Stockholm*, Fransson TH (ed.). Kluwer: Dordrecht, 1998; 211–224 (ISBN 0-7923-5040-5).
28. Kreiselmaier E, Laschka B. Small disturbance Euler equations: efficient and accurate tool for unsteady load prediction. *Journal of Aircraft* 2000; **37**:770–778.
29. Clark WS, Hall KC. A time-linearized Navier–Stokes analysis of stall flutter. *ASME Journal of Turbomachinery* 2000; **122**:467–476.
30. Chen T, Vasanthakumar P, He L. Unsteady blade row interaction using nonlinear harmonic approach. *Journal of Propulsion and Power* 2001; **17**:651–658.
31. Sbardella L, Imregun M. Linearized unsteady viscous turbomachinery flows using hybrid grids. *ASME Journal of Turbomachinery* 2001; **123**:568–582.
32. Prasad D, Verdon JM. A 3-D linearized Euler analysis of classical wake/stator interactions: validation and unsteady response predictions. *International Journal of Aeroacoustics* 2002; **1**:137–163.
33. Hall KC, Thomas JP, Clark WS. Computation of unsteady nonlinear flow in cascades using a harmonic balance technique. *AIAA Journal* 2002; **40**:879–886.
34. Campobasso MS, Giles MB. Effects of flow instabilities on the linear analysis of turbomachinery aeroelasticity. *Journal of Propulsion and Power* 2003; **19**:250–259.
35. Campobasso MS, Giles MB. Stabilization of linear flow solver for turbomachinery aeroelasticity using recursive projection method. *AIAA Journal* 2004; **42**:1765–1774.
36. Rao PP, Morris PJ. Use of finite element methods in frequency domain aeroacoustics. *AIAA Journal* 2006; **44**:1643–1652.

DOI: 10.1002/fld

37. MacCormack RW. A numerical method for solving the equations of compressible viscous flow. *AIAA Journal* 1982; **20**:1275–1281.
38. Ni RH. A multiple grid scheme for solving the Euler equations. *AIAA Journal* 1982; **20**:1565–1571.
39. Jameson A. Time-dependent calculations using multigrid, with applications to unsteady flows past airfoils and wings. *AIAA Paper 1991-1596*, 1991.
40. Roe PL. Approximate Riemann solvers, parameter vectors, and difference schemes. *Journal of Computational Physics* 1981; **43**:357–372.
41. Saad Y. *Iterative Methods for Sparce Linear Systems* (2nd edn). SIAM: Philadelphia, PA, 2003, ISBN 978-0-898715-34-7.
42. Clark WS. Investigation of unsteady viscous flows in turbomachinery using a linearized Navier–Stokes analysis. *Ph.D. Thesis*, Duke University, Durham, NC, 1998.
43. Lax PD, Wendroff B. Difference schemes for hyperbolic equations with high order of accuracy. *Communications on Pure and Applied Mathematics* 1964; **17**:381–398.
44. Jameson A, Turkel E. Implicit schemes and LU-decompositions. *Mathematics of Computation* 1981; **37**:385–397.
45. Moinier P. Algorithm developments for an unstructured viscous flow solver. *Ph.D. Thesis*, Oxford University, Oxford, 1999.
46. Saad Y. GMRES: A generalized minimal residual algorithm for solving nonsymmetric linear systems. *SIAM Journal on Scientific and Statistical Computing* 1986; **7**:856–869.
47. Shroff G, Keller H. Stabilization of unstable procedures: the recursive projection method. *SIAM Journal on Numerical Analysis* 1993; **30**:1099–1120.
48. Anderson WK, Thomas JL, van Leer B. Comparison of finite-volume flux-vector-Splittings for the Euler equations. *AIAA Journal* 1986; **24**:1453–1460.
49. Spalart PR, Allmaras SR. A 1-equation turbulence model for aerodynamic flows. *Recherche Aérospatiale* 1994; **1994.1**:5–21 (also AIAA Paper 92-0439).
50. Lax PD. Weak solutions of nonlinear hyperbolic equations and their numerical computation. *Communications on Pure and Applied Mathematics* 1954; **7**:159–193.
51. Lax PD. Hyperbolic systems of conservation laws II. *Communications on Pure and Applied Mathematics* 1957; **10**:537–566.
52. Porter RW, Coakley JF. Use of characteristics for boundaries in time-dependent finite-difference analysis of multi-dimensional gasdynamics. *International Journal for Numerical Methods in Engineering* 1972; **5**:91–101.
53. Salas MD. Shock-fitting method for complicated 2-D supersonic flows. *AIAA Journal* 1976; **14**:583–588.
54. Agarwal A, Morris PJ, Mani R. Calculation of sound propagation in nonuniform flows: suppression of instability waves. *AIAA Journal* 2004; **42**:80–88.
55. Chassaing JC, Gerolymos GA, Jeremiasz JG. GMRES solution of compressible linearized Navier–Stokes equations without pseudo-time-marching. *AIAA Paper 2006-0688*, Forty-fourth AIAA Aerospace Sciences Meeting, Reno, NV, 9–12 January 2006.
56. van Leer B. *Flux-Vector-Splitting for the Euler Equations*. Lecture Notes Physics, vol. 170. Springer: Berlin, 1982; 507–512.
57. Haugeard R. Aérodynamique 3-D Instationnaire des Turbomachines Linéarisée en Temps. *Doctorat*, Université Pierre-et-Marie-Curie, Paris, 1996.
58. Imhof M. Aérodynamique Numérique Turbulente Linéarisée en Temps. *Doctorat*, Université Pierre-et-Marie-Curie, Paris, 2000.
59. Chassaing JC. Aérodynamique 3-D et Aéroélasticité Non-Linéaire et Linéarisée en Temps. *Doctorat*, Université Pierre-et-Marie-Curie, Paris, 2002.
60. van Leer B. Towards the ultimate conservative difference scheme—V—a 2-order sequel to Godunov's method. *Journal of Computational Physics* 1979; **32**:101–136.
61. Holmes D, Mitchell BE, Lorence B. 3-D linearized Navier–Stokes calculations for flutter and forced response. In *Unsteady Aerodynamics*, *Aeroacoustics*, *and Aeroelasticity of Turbomachines—Proceedings of the 8th International Symposium*, *14–18 September 1997*, *Stockholm*, Fransson TH (ed.). Kluwer: Dordrecht, 1998; 211–224 (ISBN 0-7923-5040-5).
62. Wilcox DC. Reassessment of the scale-determining equation for advanced turbulence models. *AIAA Journal* 1988; **26**:1299–1310.
63. Pope SB. *Turbulent Flows*. Cambridge University Press: Cambridge, 2000, ISBN 0-521-59125-2.
64. Kim CS, Kim C, Rho OH. Sensitivity analysis for the Navier–Stokes equations with 2-equation turbulence models. *AIAA Journal* 2001; **39**:838–845.

DOI: 10.1002/fld

65. Gerolymos GA, Sauret E, Vallet I. Contribution to the single-point-closure Reynolds–Stress modelling of inhomogeneous flow. *Theoretical and Computational Fluid Dynamics* 2004; **17**:407–431.
66. Chassaing JC, Gerolymos GA, Vallet I. Efficient and robust Reynolds–Stress model computation of 3-D compressible flows. *AIAA Journal* 2003; **41**:763–773.
67. Gerolymos GA, Vallet I. Mean-flow-multigrid for implicit Reynolds–Stress-model computations. *AIAA Journal* 2005; **43**:1887–1898.
68. Gerolymos GA, Vallet I. Wall-normal-free near-wall Reynolds–Stress closure for 3-D compressible separated flows. *AIAA Journal* 2001; **39**:1833–1842.
69. Patel VG, Rodi W, Scheuerer G. Turbulence models for near-wall and low-Reynolds-number flows: a review. *AIAA Journal* 1985; **23**:1308–1319.
70. Gerolymos GA, Vallet I. Near-wall Reynolds–Stress 3-D transonic flows computation. *AIAA Journal* 1997; **35**:228–236.
71. van Albada GD, van Leer B, Roberts Jr WW. A comparative study of computational methods in cosmic gas dynamics. *Astronomy and Astrophysics* 1982; **108**:76–84.
72. Chassaing JC, Gerolymos GA, Vallet I. Reynolds–Stress model dual-time-stepping computation of unsteady 3-D flows. *AIAA Journal* 2003; **41**:1882–1894.
73. Arnone A. Viscous analysis of 3-D rotor flow using a multigrid method. *ASME Journal of Turbomachinery* 1994; **116**:435–445.
74. Vallet I. Aérodynamique Numérique 3-D Instationnaire avec Fermeture Bas–Reynolds au Second Ordre. *Doctorat*, Université Pierre-et-Marie-Curie, Paris, 1995.
75. van Leer B. Upwind and high-resolution methods for compressible flow: from donor cell to residual distribution schemes. *Communications on Computational Physics* 2006; **1**:192–206 (also AIAA Paper 2003-3559).
76. H Lomax THP, Zingg DW. *Fundamentals of Computational Fluid Dynamics* (1st edn). Springer: Berlin, 2001, ISBN 3-540-41607-2 (corrected 2nd printing 2003).
77. Mottura L, Vigevano L, Zaccanti M. Factorized implicit upwind methods applied to inviscid flows at high Mach number. *AIAA Journal* 2000; **38**:1846–1852.
78. Gerolymos GA, Vallet I. Implicit computation of the 3-D compressible Navier–Stokes equations using $k-\varepsilon$ turbulence closure. *AIAA Journal* 1996; **34**:1321–1330.
79. Chakravarthy SR. Euler equations—implicit schemes and boundary conditions. *AIAA Journal* 1983; **21**:699–706.
80. Golub GH, Van Loan CF. *Matrix Computations*. The John Hopkins University Press: Baltimore, MD, 1989; 150–152, ISBN 0-8018-5414-8.
81. Ott P. Oszillierender Senkrechter Verdichtungsstoß in einer ebenen Düsen. *Doctorat*, Ecole Polytechnique Fédérale de Lausanne, Lausanne, 1992 (Communication du Laboratoire de Thermique Appliquée et de Turbomachines No 18.).
82. Ott P, Bölcs A, Fransson TH. Experimental and numerical study of the time-dependent pressure response of a shock-wave oscillating in a nozzle. *ASME Journal of Turbomachinery* 1995; **117**:106–114.
83. Gerolymos GA, Vallet I, Bölcs A, Ott P. Computation of unsteady 3-D transonic nozzle flows using $k-\varepsilon$ turbulence closure. *AIAA Journal* 1996; **34**:1331–1340.
84. Gerolymos GA, Bréus JP. Computation of unsteady nozzle flow resulting from fluctuating back-pressure using Euler equations. *Aerospace Science and Technology* 1998; **2**:228–236.
85. Gerolymos GA, Neubauer J, Michon GJ. Analysis and application of chorochronic periodicity for turbomachinery rotor/stator interaction computations. *Journal of Propulsion and Power* 2002; **18**:1139–1152.
86. Délery JM. Experimental investigation of turbulence properties in transonic shock/boundary-layer interactions. *AIAA Journal* 1983; **21**:180–185 (also AIAA Paper 81-1245, 1981).
87. Warming RF, Beam RM, Hyett BJ. Diagonalization and simultaneous symmetrization of the gas-dynamic matrices. *Mathematics of Computation* 1975; **29**:53–72.
88. Smits AJ, Dussauge JP. *Turbulent Shear Layers in Supersonic Flow*. AIP Press: Woodbury, NY, ISBN 1-56396-260-8.
89. Hedstrom GW. Nonreflecting boundary conditions for nonlinear hyperbolic systems. *Journal of Computational Physics* 1979; **30**:222–237.
90. Chassaing JC, Gerolymos GA. Time-domain implementation of nonreflecting boundary-conditions for the nonlinear Euler equations. *Applied Mathematical Modelling* 2007; **31**:2172–2188.

DOI: 10.1002/fld